Materials and Interfaces

Scilight

Review

Polymer-Patched Plasmonic Nanoparticles

Chansong Kim [1], Xiaoying Lin [1], Jiyeon Kim [1], Yangming Wang [1], and Qian Chen [1,2,3,4,*]

[1] Department of Materials Science and Engineering, the Grainger College of Engineering, University of Illinois, Urbana, IL 61801, USA
[2] Materials Research Laboratory, University of Illinois, Urbana, IL 61801, USA
[3] Department of Chemistry, University of Illinois, Urbana, IL 61801, USA
[4] Beckman Institute for Advanced Science and Technology, University of Illinois, Urbana, IL 61801, USA
[*] Correspondence: qchen20@illinois.edu

Received: 3 March 2025; Revised: 22 March 2025; Accepted: 25 March 2025; Published: 29 March 2025

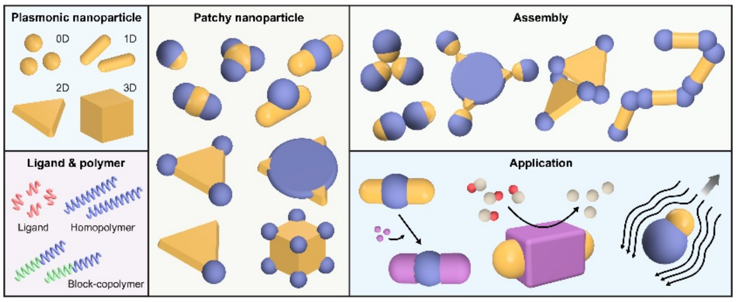

Abstract: In this work, we discuss advancements at the intersection of surface patchiness design and plasmonic nanoparticles. Surface patchiness design, inspired by nature's strategy to encode complex functions by spatially distributed surface patterns, has become increasingly popular in nanoparticle research. The surface patterns lead to their nonuniformity in chemical and physical properties, enabling not only their application as functional hybrid nanomaterials but as building blocks for self-assembly through directional interactions for applications in catalysis, biomedicine, sensing, robotics, and metamaterials. When surface patchiness design is implemented on plasmonic nanoparticles, interesting coupling of plasmonic resonance emerges from self-assembly structures not easily available from non-patchy nanoparticles. This direction is rapidly evolving and we review efforts in the synthesis, self-assembly, and applications of plasmonic patchy nanoparticles. We conclude with outlook discussions of the future opportunities of this field.

Keywords: patchy nanoparticles; plasmonic particles; polymer ligands; surface chemistry; self-assembly

1. Introduction

Inorganic nanoparticles (NPs) such as metal oxides and noble metals have been extensively studied over the last few decades due to their chemical stability against oxidation and degradation, the convenience to achieve surface modification for attachments of functional groups, and size-dependent electromagnetic properties [1–4]. In particular, plasmonic NPs, such as Au and Ag, exhibit localized surface plasmon resonance (LSPR), which arises from the collective oscillation of free electrons in the metal resonating upon excitation of electromagnetic wave at a specific wavelength [5,6]. Based on LSPR effect, plasmonic NPs are widely used in catalysis [7], sensing [8], and photothermal therapy [9]. Furthermore, self-assembly of these plasmonic NPs can have plasmon coupling dependent on the details of assembly structure, involving both local and global symmetry, which are distinctive from a simple sum of the SPRs of individual NPs [10]. Take a dimeric assembly of NPs—the simplest assembly of two NPs—as an example. For Au nanospheres (NSs), the LSPRs are sensitively dependent on the distance of the two NPs, which is the design principle of plasmonic rulers [11,12] capable of measuring local chemical reactions and distances at nanometer precision. For shape-anisotropic NPs, such as Au triangular prisms, the "bow-tie" configuration of dimers [13], where the sharp tips of each prism are positioned close or in contact with each other, can have a "hot spot", namely an immensely enhanced electromagnetic field around the tip regions, useful for nanoantenna arrays, near field optics, and sensing. It is for the importance of assembly structures in plasmonic coupling that researchers have extended different strategies of making self-assembly structures. One strategy that has gained increasing attention is through surface patchiness design on plasmonic NPs to make the patches repulsive or attractive for directing the self-assembly into nonconventional structures such as non-closely packed structures, and for controlling the relative orientation of contacting pairs of NPs, thereby expanding the applications of NP assemblies. Moreover, surface patterning of NPs by ligand molecules is a powerful strategy to introduce functionalities in addition to those of the core NPs, allowing more dimensions of control in properties such as wettability, surface charge density, bio-specificity, host-guest interaction, and mechanical stiffness.

For plasmonic patchy NPs, a key challenge has been on the synthesis, as it is hard to achieve high precision in patterning ligand molecules on a NP surface with nanometer precision. For colloidal particles that are micrometer in size, various top-down methods such as electron beam lithography and deposition have been utilized to coat the particles with surface patches [14–16], thereby enabling directional self-assembly [16,17] and diverse applications such as biomedicine [18], sensing [19], self-propelling motors [20,21], and anti-counterfeiting [22]. However, most of these methods have a resolution that is around tens to hundreds of nanometer resolution [23,24], not sufficient for NPs. In the field of microelectronics, surface chemistry patterning has been vigorously pushed for advancements in spatial resolution, for ever-smaller and fast chip technology. Yet even aided with bottom-up assemblies such as polymer microphase separation, current patterning on these chip-based microelectronics has a pitch size of 7 nm and are mostly applied to flat substrates [25].

Thus, the focus of this article (Figure 1) is on highlighting achievements in the synthesis of patchy plasmonic NPs with high precision, particularly on polymer-coated patchy NPs. The formation of polymer patches is intricate, considering both the ligand−NP interactions through chemisorption or physisorption, as well as the polymer−polymer, polymer−solvent interactions which determine the chain configurations, patch dimension, and patch shape. Next, we discuss efforts on the self-assembly of polymer-patched NPs directed through either patch−patch attraction or repulsion. We also discuss current effort to utilize patchy plasmonic NPs in practical applications Finally, we provide our perspectives of the remaining challenges and opportunities for the areas of plasmonic patchy NPs.

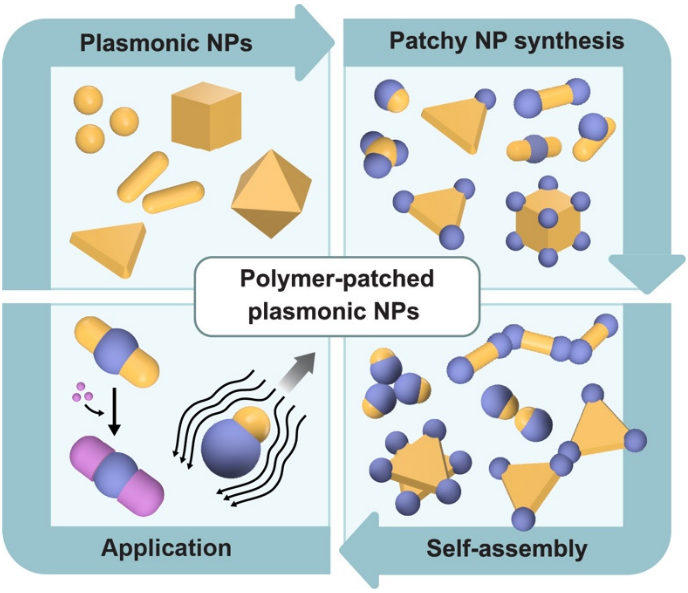

Figure 1. Schematic illustration of the overview of this work. Plasmonic NPs with various shapes can be used to synthesize patchy NPs. These patchy NPs can serve as building blocks for assemblies via directional interactions into a diversity of assembly structures. Due to the surface patchiness, patchy NPs can be used for practical applications such as templates for site-selective depositions and self-propelling nanomotors.

2. Synthesis of Patchy Plasmonic NPs

This section covers the methods used in synthesizing polymer-patched plasmonic NPs, mostly Au NPs, classified into six categories based on the synthesis mechanisms: (1) solvent-mediated segregation of homopolymer ligands, (2) solvent-mediated segregation of block copolymer ligands, (3) microphase separation of ligands, (4) heat-induced transformation of polymer ligands, (5) site-selective binding of ligands, and (6) other strategies such as plasmonic-induced patch formation and templated surface modification.

2.1. Solvent-Mediated Segregation of Homopolymers

Polymer molecules with a functional group that can chemically bind to noble metal NPs, through Au−thiol and Au−amine bonds, are widely used to synthesize polymer-coated NPs since the strong chemical bonds ensure stable surface modification of NPs. These polymer ligands can exhibit different phase behaviors such as swelling and collapsing, depending on the solvents, to balance polymer−solvent interfacial energy and polymer−polymer interaction [26]. Thus for the synthesis of polymer-patched NPs, the phase transition of polymer ligands collapsing into segregated surface patches was among the first successful strategies.

This strategy was pioneered by Kumacheva and coworkers, when they reported a milestone in the synthesis of patchy plasmonic Au and Ag NPs by utilizing solvent-mediated polymer segregation of homopolymer ligands [27]. Specifically, they first grafted NPs with hydrophobic thiol-terminated polystyrene (HS-PS) ligands in dimethylformamide (DMF), which is a good solvent for the ligands. In DMF, the ligands fully cover the NP surface and are extended with favored solvent−polymer contact. Then the solvent quality was reduced by adding controlled portion of poor solvent, water, for the polymer ligands, to cause collapsing of the grafted polymer ligands into spatially discrete, pinned micelles as polymer patches on the NP surface. These pinned micelles consisted of dense cores of aggregated polymers and stretched surface-tethered 'legs', the latter of which serve as polymer bridges between core NPs and densely collapsed patches. This polymer segregation was governed by the balance between the polymer−solvent interfacial energy and the stretching energy of the micellar 'legs.' In the Au NS system, for example, transition from core−shell to patchy structures is favored at decreasing polymer grafting density (σ) and core NP diameter (D). At high σ, the extended polymer chains minimize their interfacial and stretching energies by forming a smooth layer, which resulted in homogeneously coated Au core−polymer shell NPs. In contrast, at lower σ, the polymer coating becomes thinner, and the interfacial energy is lowered by polymer segregation into pinned micelles. Additionally, the competition between the polymer–solvent interfacial energy (favoring segregation) and the elastic energy of stretched micellar 'legs' (favoring core−shell coating) determines the optimized pinned micelle footprint area (A), which is proportional to $(N^2/\sigma)^{2/5}$, where N is the polymer degree of polymerization. It was demonstrated that the number of pinned micelles per NP (n) is proportional to the ratio between the surface area of Au NS (πD^2) and A, which suggests that the ratio of D to polymer chain size (R, defined as the root-mean-square end-to-end distance of a polymer in its ideal conformation) (D/R) determine the number and spatial distribution of patches.

After this pioneering work, similar strategies were extended to different anisotropically shaped NPs. One prominent example is one-dimensional (1D) Au nanorods (NRs), which unlike Au NSs, exhibit different local surface curvatures along the Au NP in two principal axis directions: a cylindrical segment with zero curvature along the longitudinal axis and positive curvature along the transverse axis [28]. By reducing solvent quality, Kumacheva and coworkers show that Au NRs with polymer ligands uniformly grafted can form diverse NP structures, such as core−shells, discrete random patches, and helicoidal patch arrangements, depending on the lN, where l is monomer length, surface curvature ($1/r$, where r is radius of the fitted circle of the Au NR surface), and σ (Figure 2a,b). Notably, the formation of the helicoidal patches with handedness was a surprise and differs from uniformly collapsed patches in most cases.

This breaking of symmetry was rationalized by the two different curvature values, which govern the formation of polymer-pinned micelles upon reduced solvent quality on Au NRs. On one hand, the footprint of pinned micelles elongates in the direction parallel to the Au NR long axis. On the other, perpendicular to the Au NR long axis, the stretched polymer micelles experience a high local curvature and become connected with each other at the centers of the nearest micelles. With these two effects combined, in the end, the patches twist at an angle with respect to the long axis, and coalesce along the line of the shortest distance between the neighboring patches, resulting in the helicoidal patch structure (Figure 2c).

Given the importance of local surface curvature of the core NP in determining the patch patterns, more follow-up studies focused on the gradual evolution of patch patterns occurred while the shape of the core NPs changes, accompanied by changes in local surface curvature [29]. When Au NPs are exposed to Au^{3+} ions in an aqueous solution of cetyltrimethylammonium bromide (CTAB), Au^{3+}−CTAB complexes form, and they can etch the Au NPs through comproportionation reaction [30]. Kumacheva and coworkers used this straightforward chemistry to induce the etching of patchy Au nanocubes (NCs) after the patchy particles were synthesized following solvent quality-induced polymer segregation strategy. During this etching process, Au NCs gradually transformed into Au NSs, leading to changes in the shape and number of patches on the NPs. The patch patterns on the etched Au NCs resemble those on patchy Au NSs directly synthesized via the polymer segregation of polymer ligands. While Au NCs exhibited eight corner patches from the transmission electron microscopy (TEM) images (only four shown due to two-dimensional projection, Figure 2d), three patches were observed on both etched Au NCs and Au NSs (Figure 2e). This similarity of patch patterns between the etched Au NCs and Au NSs highlighted again the critical role of local surface curvature of the core NPs on determining the patch patterns.

In addition to in-situ etching, the patch pattern changes can also occur through the ligand migration. In the examples above, thiol-terminated polymer ligands, such as HS-PS, have been utilized to exploit Au−thiol bonds. It is well known that the barrier for desorption of thiol-terminated molecules on Au surfaces are 20–50 $k_B T$ in solution [31,32], with the barrier for lateral migration of the molecules along Au surface even lower. Thus it was hypothesized that thermal treatment can induce the migration of polymer patches. Indeed, work by Kumacheva and coworkers show that the polymer patterns on Au NPs can change upon heating [33]. In this study, Au NSs with two patches were firstly prepared and then incubated for different time durations at varying temperatures to observe the patch shape transformation. While no obvious change was found at low temperature (25 and 40 °C) even after 96 h of incubation due to insufficient thermal energy, gradual transformation of polymer patterns into one-patch and even complete loss of patches (due to thiol desorption) after 2 days and 4 days of incubation at 80 °C, respectively (Figure 2f).

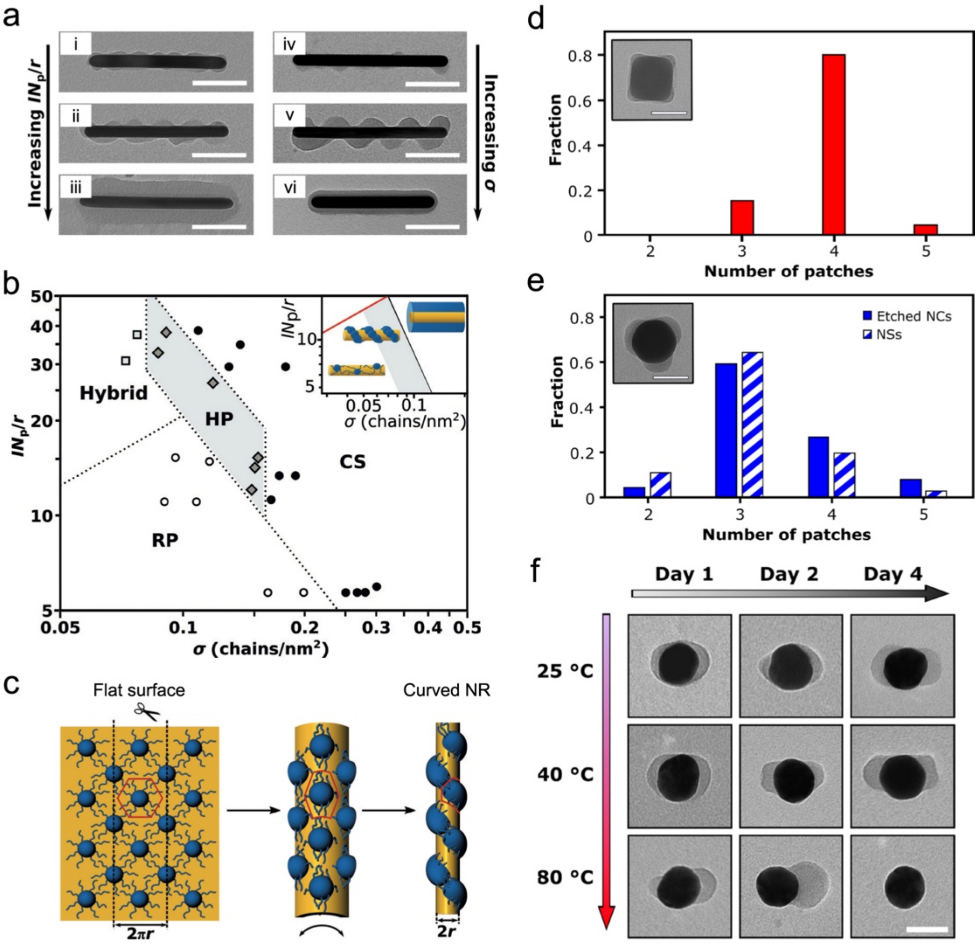

Figure 2. Solvent-mediated segregation of homopolymer ligands on anisotropically shaped Au NPs. (**a**) Representative TEM images of patchy Au NRs synthesized under varying lN/r and σ. (**b**) Experimental diagram of polymer pattern states as a function of lN/r and σ for the Au NRs. (**c**) Schematic illustrating the formation of the helicoidal patches on NRs. (**d**,**e**) Histograms of patchy Au NCs (**d**), as well as etched Au NCs and Au NSs (**e**) with different n. (**f**) Representative TEM images of patchy Au NSs after thermal treatment at different temperatures for varying durations. Scale bars: (**a**) 100 nm, (**d**,**e**) 50 nm, and (**f**) 40 nm. (**a**–**c**) Reproduced with permission from ref. [28]. Copyright 2019, Wiley-VCH. (**d**,**e**) Reproduced with permission from ref. [29]. Copyright 2017, American Chemical Society. (**f**) Reproduced with permission from ref. [33]. Copyright 2020, American Chemical Society.

2.2. Solvent-Mediated Segregation of Block Copolymers

The above early synthetic efforts of patchy NPs using the solvent-mediated polymer segregation strategy primarily employed homopolymer ligands such as HS-PS for patch formation. However, when polymer ligands segregate due to reduced solvent quality, the stability of the NPs can also be compromised. This reduced stability can lead to agglomeration of polymer-patched NPs due to the lack of inter-NP repulsion. Consequently, these patchy NPs often require precise control over the solvent quality and are typically synthesized under low NP concentrations, with relatively low yield. To mitigate these challenges, block copolymer ligands were used as a good ligand candidate for synthesizing patchy NPs using the polymer segregation strategy, with the ligands consisting of at least two blocks: a NP-adjacent block that forms patches, and a NP-remote block that stabilizes the patchy NP in the solvent. Furthermore, since this NP-remote block governs the stability of patchy NPs, they also determine the subsequent assembly of the patchy NPs.

Kumacheva and coworkers pioneered the usage of end-grafted block copolymer ligands to synthesize patchy Au NPs with enhanced stability [34]. A trithiocarbonate-terminated block copolymer, consisting of a PS block (a NP-adjacent block for patchy formation) and a poly(4-vinylbenzoic acid) (P4VBA) block (a NP-remote block for the stabilization and subsequent self-assembly) was used to coat Au NPs uniformly first, followed by a reduction in solvent quality. A trithiocarbonate-terminated PS homopolymer ligand was also used as a control sample for comparison. Under poor solvency conditions, Janus structures formed for both ligands through polymer segregation. However, the reduced solvent quality compromised the stability of homopolymer ligand-grafted Au NPs, leading to simultaneous formation of merged patchy Au NPs, with limited control over synthesis. In contrast, block copolymer ligand-grafted Au NPs exhibited stable patchy structures and good NP dispersibility in poor solvents, allowing subsequent self-assembly (Figure 3a).

Since this pioneering work, various block copolymers have been used for synthesizing patchy NPs to utilize the functionality of different polymer blocks. He and coworkers synthesized patchy NPs using a mixture of homopolymer ligands and block copolymers [35–37]. Hydrophobic HS-PS and amphiphilic block copolymer, such as PS-*b*-poly(acrylic acid) (PS-*b*-PAA) and PS-*b*-poly(ethylene oxide) (PS-*b*-PEO), were introduced into Au NSs in a mixture of DMF and water [35,36]. When HS-PS was first grafted on the Au surface, water in the solvent mixture induced polymer segregation and site-selective surface decoration. The block copolymer with a PS block then bound to the pre-attached HS-PS via hydrophobic attractions, thereby forming Janus patches (Figure 3b). Importantly, these block copolymer-coated NPs can stay stabilized due to the hydrophilic block, even in water which is a poor solvent for PS block. The polymer patterns on the NPs were determined by the concentration of the polymer ligand. Under low HS-PS concentrations, Janus structures formed, while fully covered NPs were observed under high HS-PS concentration. Patch coverage decrease, showing gradual transitions from core–shell to patchy structures, was observed as the polymer ligand concentration decreased (Figure 3c). This synthesis method was also applied to other shaped particles. Interestingly, when using NRs, a dumbbell-like patch pattern with two patches at both NR ends formed at low HS-PS concentrations [37]. The higher local curvature at the ends than those along the rods resulted in a smaller polymer–solvent interface, leading to site-selective polymer grafting at the NR ends (Figure 3d). Furthermore, as the concentration of anchoring HS-PS decreased further, a gradual transition from individual dumbbell-like structures to interlinked 1D chain-like assemblies were formed, with decreasing end-to-end distances due to lower σ (Figure 3d). Notably, this decreased end-to-end distance resulted in a red shift of the longitudinal LSPR due to the plasmon coupling effect.

In addition to block copolymers, patchy Au NPs have been also synthesized with a thiol-terminated block-random copolymer ligand, consisting of three different segments—hydrophilic PEO, hydrophobic PS, and a randomly copolymerized blocks [38]. By using this block-random copolymer ligands, Nie and coworkers achieved not only enhanced stability of patchy Au NPs while reducing solvent quality but also a broader library of patch patterns, which were difficult to achieve using diblock copolymers. The structural evolution from fully coated polymer ligands to patches was attributed to the molecular exchange between the polymers on Au NP surface and the free polymer micelles in the solution upon sequential reducing solvent quality and heating at 110 °C. When water, a poor solvent for the hydrophobic PS block, was added to the solution of fully coated Au NPs, patchy structures were formed by polymer segregation. Upon heating, dynamic ligand exchange led to the evolution of patch shapes, making patch sizes more uniform and distributing them more symmetrically on the Au NP surface over time (Figure 3e). Notably, the presence of the randomly copolymerized block regulated this dynamic molecular exchange, acting as a buffering region between the hydrophilic and hydrophobic blocks. Through this method, diverse patchy Au NPs with controlled morphology and different n, such as beanlike patches, one-, two-, three-, and multiple-patches ($n > 3$), were formed (Figure 3f).

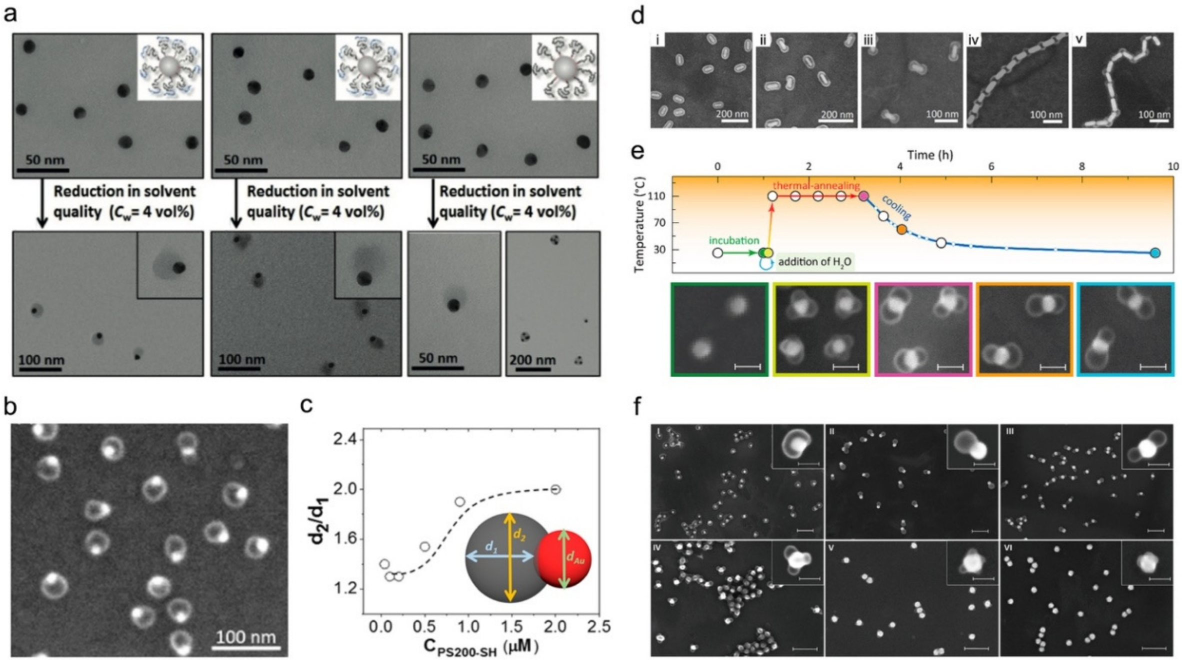

Figure 3. Solvent-mediated segregation of block copolymer ligands on Au NPs for patch formation. (**a**) Representative TEM images of Au NPs coated with short (left) and long (middle) PS-*b*-P4VPA block copolymer ligands, and a PS homopolymer ligand (right), before and after reducing solvent quality. (**b**) Representative scanning electron microscopy (SEM) image of Janus Au NPs with PS-*b*-PEO patches. (**c**) The changes in the d_2/d_1 ratio of the Janus Au NPs shown in (**b**) under varying HS-PS ligand concentrations. The inset schematic defines d_1 and d_2. (**d**) Representative SEM images of patchy Au NRs prepared at decreasing HS-PS polymer ligand concentrations (from left to right). (**e**) Schematic of the patch formation process and SEM images showing the morphological evolution of the patches. The colored boxes in each SEM image correspond to the experimental conditions indicated by data points of the same color in the schematic. (**f**) Low- and high-magnification (insets) SEM images of patchy Au NPs with different morphologies synthesized using a block-random copolymer. Scale bars: (**e**) 50 nm and (**f**) 200 nm (insets: 50 nm). (**a**) Reproduced with permission from ref. [34]. Copyright 2019, Wiley-VCH. (**b**,**c**) Reproduced with permission from ref. [35]. Copyright 2021, American Chemical Society. (**d**) Reproduced with permission from ref. [37]. Copyright 2023, American Chemical Society. (**e**,**f**) Reproduced with permission from ref. [38]. Copyright 2021, American Chemical Society.

2.3. Microphase Separation-Induced Patch Formation

Even though controllability of patch patterns was achieved using copolymers, most solvent-mediated strategies for patchy NP synthesis utilizing one kind of ligand still exhibited limited patch patterns. Usually, only a single type of patch structure could be formed on a given core NP shape, such as Janus for NSs and end-grafting for NRs. Furthermore, the solvent-mediated synthesis method utilizes polymer strand collapse on fully polymer-coated NPs grafted with a single type of polymer. Thus efforts reviewed in this section focused on having more than one ligand.

When multiple thiol-terminated ligands are grafted on one NP, spontaneous microphase separation of the mixed polymer ligands can occur through their lateral diffusion to maximize their conformational entropy gain as well as enthalpic attraction sites. The number, size, and spatial distribution of each polymer domain are determined by the structural properties of the core NPs such as surface curvature, the chemical structures of ligands such as length and bulkiness, and the molecular ratio of each species [39,40]. This microphase separation has been utilized to synthesize patchy NPs. Chen and coworkers reported the patchy Au NSs synthesized using a binary mixture of thiol-terminated ligands with different hydrophilicities (2-dipalmitoyl-*sn*-glycero-3-phosphothioethanol for a hydrophobic ligand and either diethylamine or 2-mercaptoacetic acid for a hydrophilic ligand) along with block copolymer [41]. The two ligands bound to the Au NP surface, forming separated ligand domains. The PS-*b*-PAA block copolymer then attached site-selectively to the hydrophobic ligand-coated regions via hydrophobic attraction. Notably, it was demonstrated that the concentration ratio of hydrophobic to hydrophilic ligands (L_A/L_B) determined the morphology of polymer patch patterns on the NP surface. The homocentric core–shell structure gradually transitioned into a slightly eccentric and then a highly eccentric Janus shape as the L_A/L_B ratio decreased (Figure 4a). This transition was attributed to the formation of small hydrophobic domain on the surface under relatively deficient hydrophobic ligand concentrations, where the PS block of the PS-*b*-PAA molecules can attach via hydrophobic attraction. Interestingly, sequential addition of a hydrophobic ligand after the incubation of Au NPs with a hydrophilic ligand, instead of using a mixture of hydrophobic and hydrophilic ligands for ligand grafting, resulted in flower-like patchy structures exhibiting multiple patches on NP surfaces. This was attributed to uneven distribution of hydrophobic ligands on Au NPs, resulting from the kinetically controlled dissociation of pre-attached hydrophilic ligands from the Au NPs and ligand exchange with hydrophobic ligands in solutions.

The underlying mechanism of microphase separation-driven patchy NP formation was proposed based on a three-phase wetting problem, which involves the balance of three interfacial free energies: NP–solvent, NP–polymer, and polymer–solvent [42]. Depending on their relative magnitudes, the polymer chains either completely or partially covered the NP surface. This resulted in different polymer patch patterns, as they preferentially coated on the hydrophobic ligand domains to minimize the overall free energy. Specifically, NP–solvent interfacial energy is determined by the hydrophilicity of the NP, which is governed by the ligand chemistry, namely the L_A/L_B ratio. When the NP surface was coated with hydrophobic ligands exclusively in a polar solvent, the NP–solvent interfacial energy increased, resulting in a fully polymer-coated core–shell structure to minimize interfacial area between NP and solvent. In contrast, as more hydrophilic ligands covered the NP surface, the lower NP–solvent interfacial energy led to partial coverage, thereby forming patchy structures. Based on this wetting-induced microphase separation, structural diversity in patchy Au NPs was achieved by controlling the L_A/L_B ratio. This microphase separation for synthesizing patchy NPs effective for different ligand mixtures, yielding distinct patch patterns such as periodic patches on Au NRs when using a mixture of HS-PS and HS-methoxy PEO (mPEO) (Figure 4b) [43], and differently shaped core Au NPs including spheres, rods, triangular prisms, cubes, and octahedra [42,44].

In addition to microphase separation induced only by physical, non-covalent interactions, in situ self-polymerization of dithiol ligands can induce patch formation on NPs through microphase separation by using it along with other ligands [45]. For example, benzene-1,4-dithiol (BDT) can create a polymer layer on Au NPs via self-polymerization. Specifically, when BDT molecules attach to the Au surface, additional BDT molecules subsequently bind to the pre-attached BDT through disulfide bridging, thereby forming polymerized BDT (pBDT). This process also facilitates further polymerization on pre-attached BDT and/or pBDT via π−π stacking. The Au NPs used in this study were initially stabilized by sodium dodecyl sulfate (SDS) in solution. Thus, the BDT polymerization on the Au NPs was initiated through ligand exchange between SDS on the Au NP surface and BDT in solution, making a similar scenario to that in which multiple ligands showing different hydrophilicity induce microphase separation on the surface. Consequently, this process, akin to microphase separation, resulted in Janus Au NPs. Moreover, beyond this BDT unary ligand system, binary and ternary ligand systems incorporating multiple ligands were also employed with varying ligand types and molar ratios (Figure 4c–h). The use of BDT alongside multiple ligands, such as 4-methylbenzenethiol (MBT), 4-mercaptophenol (MCP), 4-mercaptobenzoic acid (MBA), and 4-aminothiophenol (ATP), enabled various patch structures. These patch patterns were governed by the ligand types and molar ratio of each species, ranging from simple Janus structures to complex patch shapes with different n. Additionally, the study on the time-dependent transformation of polymer patterns using a binary system of BDT and ATP confirmed the underlying mechanism of self-polymerization-driven patch formation. After creating multiple patches on the Au NP at the beginning of the reaction, the number of patches gradually decreased over time, eventually resulting in two-patch structure (Figure 4g). It is likely that the electrostatic repulsion between patches on the confined Au NP surface increased as the patches grew larger, thereby limiting their further growth. To overcome this barrier, existing small patches dissociated and reorganized into a larger patch to lower the surface energy. This demonstrated that, in addition to surface binding energy (between core NP and grafting ligands) and π−π interaction (between ligands), which are known to govern microphase separation, additional interactions, such as patch−patch electrostatic repulsion, can also influence the patching reaction.

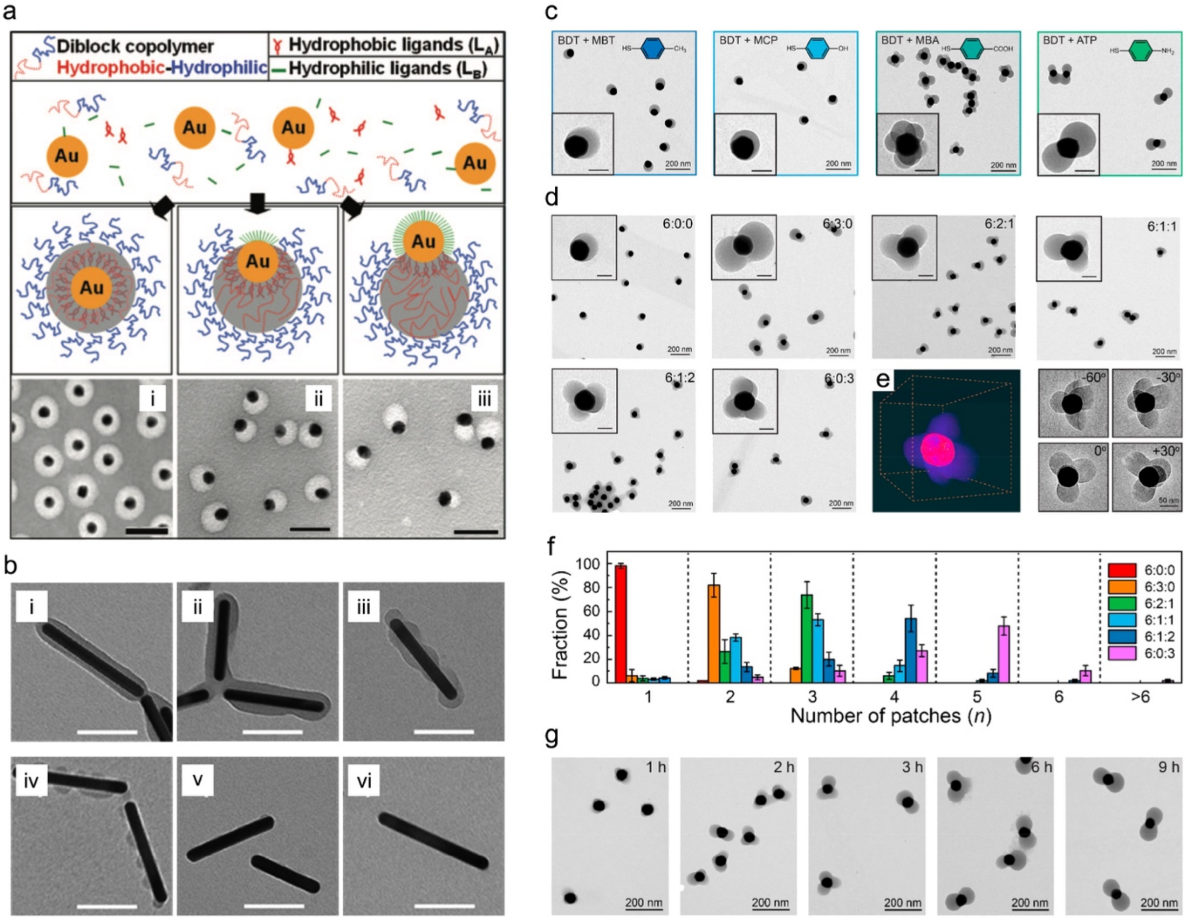

Figure 4. Microphase separation of ligands inducing patch formation on Au NPs. (**a**) Schematic and representative TEM images showing the formation of homocentric (**left**) and eccentric (**middle** and **right**) polymer patterns on Au NPs at increasing L_A/L_B ratios (from **left** to **right**). (**b**) TEM images of patchy Au NRs synthesized using a mixed hydrophobic HS-PS and hydrophilic HS-mPEO at increasing L_A/L_B ratios (from **i** to **vi**). (**c**,**d**) Low- and high-magnification TEM images of pBDT patchy Au NSs synthesized under a binary (with varying ligand type) (**c**) and a ternary (at varying molar ratios between ATP and MBA) (**d**) ligand systems. The values in (**d**) represent the molar ratio of BDT:ATP:MBA. (**e**) 3D electron tomography reconstruction of a patchy Au NS coated with four patches obtained with a stoichiometric ratio of 6:1:2, along with corresponding TEM images at different tilting angles. (**f**) Histogram of patchy Au NSs with different n in each stoichiometric ratio. (**g**) TEM images of patchy Au NSs at different time of reaction, showing the transition of patch configurations. Scale bars: (**a**) 50 nm, (**b**) 100 nm, and (**c**,**d**) 50 nm. (**a**) Reproduced with permission from ref. [41]. Copyright 2008, American Chemical Society. (**b**) Reproduced with permission from ref. [43]. Copyright 2019, American Chemical Society. (**c**–**g**) Reproduced with permission from ref. [45]. Copyright 2021, American Chemical Society.

2.4. Heat-Induced Transformation of Polymer Coatings on NPs to Form Patches

As noted in Section 2.1, the patch patterns formed from solvent quality reduction in homopolymer ligands of HS-PS can be changed upon heat treatment. The same principle can be applied to other more complex systems. For example, when polymer coatings are formed on the Au NP surface using thiol-terminated hydrophobic ligands and amphiphilic block copolymers, the ligands first bind to Au NP surfaces, followed by the attachment of the block copolymers through hydrophobic attractions between ligands and the hydrophobic block of block copolymers. In this case, sufficient thermal energy at elevated temperature can "liquefy" the polymer coating by weakening the ligand–polymer attractions, leading to the formation of polymer patch patterns on NPs. Therefore, this heat-induced transformation of polymer coatings has been broadly used for synthesizing patchy Au NPs.

Chen and coworkers used this strategy to synthesize patchy Au NRs which formed with diverse types of thiol-terminated ligands alongside PS-*b*-PAA, at sufficiently high temperature [46]. Upon heating above 90 °C, polymers increase their mobility, leading to different transformation, such as contraction, dissociation, and winding depending on the ligand types. The controllability achieved by the hydrophobic ligand types is made possible due to variations in intermolecular interactions between polymer and ligands. Specifically, 2-

naphthalenethiol (2-NAT) (Figure 5a) and biphenyl-4-thiol (Figure 5b) ligands have strong attractions with PS-*b*-PAA, making the polymers difficult to dissociate and thus persist on the NP surface even heated at 115 °C. Instead, the contraction of the polymer coating occurs in this case, leading to smaller sized patches (Figure 5c, left). In contrast, aliphatic (1-dodecanethiol and 1-octadecanethiol) or bulky ligands (HS-PS) have weaker attraction with PS-*b*-PAA. As a result, even heating at 90 °C, the polymers can dissociate from the ligands, with patches dislodging and moving into the aqueous phase (Figure 5c, middle). On the other hand, amphiphilic 2-dipalmitoyl-*sn*-glycero-3-phosphothioethanol interacts with PS-*b*-PAA block polymers to form micelle-like polymer domains upon heating at 60 °C, leading to winding cylinder structures (Figure 5c, right). In addition to ligand types, heating temperature and ligand concentration also influence the final patch structures.

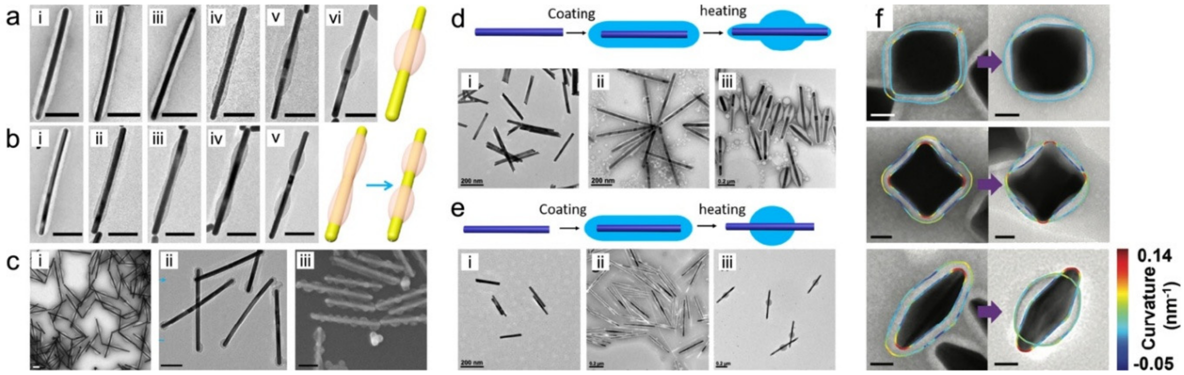

Figure 5. Heat-induced transformation of polymer coating for patch formation on NPs. (**a**,**b**) Schematics and TEM images of the initial core–shell structures and the transformation of polymer layers on Au NRs based on contraction mode, forming one- (**a**) and two-patch (**b**) structures, through thermal treatment at a temperature range of 105 to 115 °C and at 90 °C, respectively. Increased thermal energy was supplied from left to right by either extending the heating time or raising the temperature. (**c**) Representative TEM and SEM images of NRs with one-patch structure (**left**, contraction mode), two-patch at both ends (**middle**, dissociation mode), and helicoidal patch (**right**, winding mode) structures. (**d**,**e**) Schematics and TEM images of polymer shell transformation on Te NWs coated with long (**d**) and short (**e**) HS-PS polymer ligands upon heating at 80 °C. (**f**) TEM images of PS-*b*-PAA-coated NPs with different Au core shapes—octahedron (**top**), concave cube (**middle**), and bipyramid (**bottom**)—before (**left**) and after (**right**) heating. Scale bars: (**a–c**) 100 nm and (**f**) 20 nm. (**a–c**) Reproduced with permission from ref. [46]. Copyright 2018, Springer Nature. (**d**,**e**) Reproduced with permission from ref. [47]. Copyright 2019, American Chemical Society. (**f**) Reproduced with permission from ref. [48]. Copyright 2018, Wiley-VCH.

The heat-induced patch formation mechanism using thiol-terminated ligands and physisorbed polymers onto them extends to NPs of another composition, Te nanowires (NWs) (Figure 5d,e) [47], and other Au NP shapes including bipyramid, octahedron, and concave cube (Figure 5f) [48]. Notably, when one extends the patching strategy to other shapes, characterization of the patch patterns becomes non-trivial. TEM and SEM images are usually used to classify the products. Chen and coworkers customized an automated workflow to analyze many TEM images of polymer-coated Au NPs before and after segregation by recognizing the patch domain (lighter contrast in TEM images) and the core NP domain (darker contrast TEM images) first through thresholding [48]. After segmenting the core Au NP and polymer regions, they quantified a series of geometric metrics such as the thickness and local surface curvature of the polymer patches (Figure 6a). Polymer segregation into patches measures a broad range of both positive and negative values in the local curvature distribution of the patches, as a means to quantify the patch shape. From the quantitative analysis, in this work, both the thickness and local curvature of the polymer patches were higher at the high curvature regions of core Au NPs, such as the vertices of octahedra and the vertices and edges of cubes, indicating that patches were preferentially formed in NP surface regions with high surface curvature during solvent-mediated polymer segregation (Figure 6b,c).

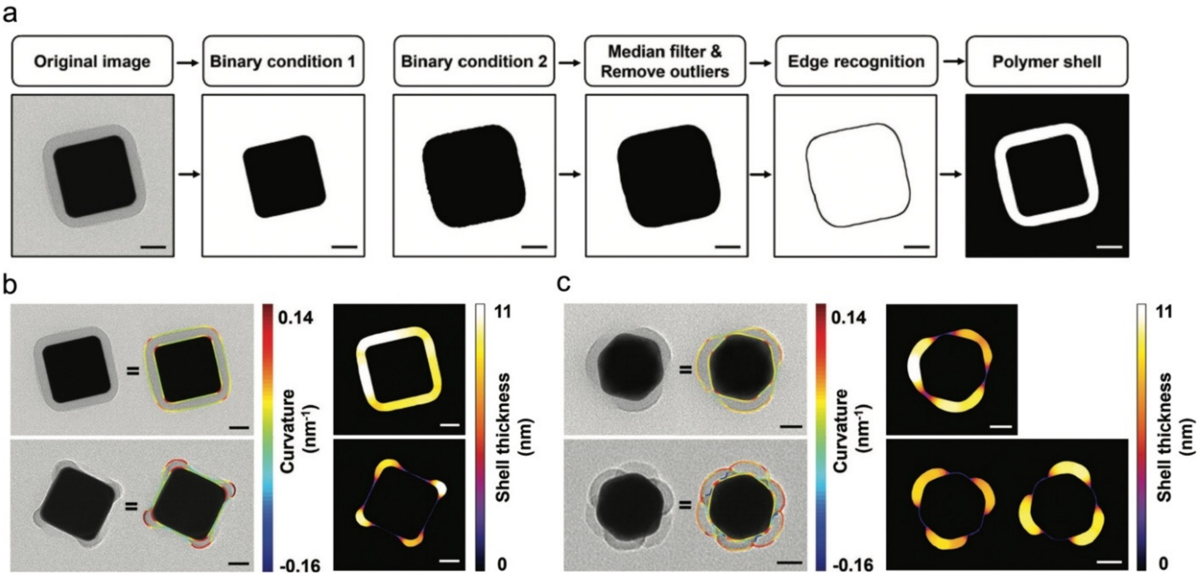

Figure 6. Image analysis of polymer-grafted NPs. (**a**) Image processing workflow for the TEM images of polymer-coated Au NPs. Analysis of local surface curvature and thickness of polymer layers based on TEM images for (**b**) cube and (**c**) octahedron system before (**top**) and after (**bottom**) segregation. The local surface curvature was defined as the inverse of the radius of the best-fitted circle to the local arc. The patch thickness was defined as diameter of the largest circle that incorporates the pixel belonging to the polymer patches. Scale bars: (**a**) 20 nm. Reproduced with permission from ref. [48]. Copyright 2018, Wiley-VCH.

2.5. Site-Selective Ligand Binding onto NPs to Form Patchy NPs

For the strategies discussed in Sections 2.1, 2.2, and 2.4, polymers uniformly adsorb onto the NP surface first and then rely on different mechanisms to either change their configurations to cluster into patches or migrate to form into domains. In this section, we focus on the methods that allow polymers to adsorb in a site-selective manner from the beginning for patchy NP formation.

Site-selective binding of ligands (small molecules or polymers), even in the absence of the microphase separation mechanism discussed in Section 2.3 was predicted to be possible given a generic balance between entropic and enthalpic effects for the ligand molecules. Glotzer and coworkers theoretically demonstrated that ligands packed at different curvature sites on a NP surfaces exhibit different configurational entropy, leading to curvature-dependent site-selective grafting of ligands on NP surfaces [49]. When ligands are tethered to different sites on polyhedral NP surface—faces, edges, and vertices—they exhibit different sizes of free volume, defined as the volume of the Voronoi cell within which they move freely in a self-avoiding random walk. Among these sites, ligands tend to attach to vertices, which exhibit the highest surface curvature, with the greatest entropy gain due to the largest Voronoi cell, compared to those attached to the edges and faces (Figure 7a). Consequently, this preference leads to a heterogenous ligand coating on NPs, which can be exploited for synthesizing patchy NPs.

In efforts translating this theoretical calculation to practical effects, the entropically-favored vertex patches were first demonstrated. For example, Chen and coworkers synthesized tip-patched Au triangular nanoprisms using a hydrophobic ligand (2-NAT) and PS-*b*-PAA block copolymer [50]. Similarly to the studies discussed in Section 2.4, the thiol-terminated ligands bind to the Au NP surface first, and the PS-*b*-PAA adsorbs onto the thiol ligands due to hydrophobic attraction. The difference is that the ligands preferentially bound to the tips of Au nanoprisms from the beginning, which exhibit significantly higher surface curvature than the rest of the prisms, to maximize the entropy gains of ligands. Subsequent adsorption of the PS-*b*-PAA polymers to the hydrophobic ligand-coated sites led to a high yield of tip-patched Au nanoprisms (Figure 7b). The patch coverage was finely controlled by ligand concentration. As the ligand concentration increased under a fixed concentration of NPs, the lateral size of the patches grew larger, leading to a gradual transformation in the patch patterns, from small tip-patches, large tip-patches to T-shaped, and eventually Reuleaux triangular patch shapes (Figure 7c). This increase in patch coverage was attributed to the expansion of ligand islands from the initial adsorption site (tips), which provided more binding sites for polymer strands as the ligand concentration increased.

As a follow-up study, Chen, Glotzer, and coworkers further studied the enthalpic effects. In this 2-NAT and PS-*b*-PAA block copolymer system, the enthalpy, or chain–chain attraction of PS-*b*-PAA is more dominant under certain reaction conditions [51]. It was demonstrated that the reaction temperature governed the symmetricity of patch shapes by controlling n on Au nanoprisms. While symmetric three tip-patches are formed at high temperature of 110 °C, a gradual decrease in n was observed as the reaction temperature decreased to finally 90 °C, which result in asymmetric one- or two-patchy structures (Figure 7d). A theoretical model based on polymer scaling theory rationalized this temperature-dependence of the patch shapes. This model incorporated both entropic and enthalpic energies resulted from the polymer chain localization on NP surfaces. The Flory-Huggins parameter, χ parameter, which is inversely proportional to temperature, was predicted to exhibit a critical value χ_c for patch patterning. Physically, polymer chain−chain attraction increased with increasing χ parameter. When $\chi > \chi_c$, the chain−chain attractions became strong enough to overcome both competing enthalpic gains associated with chain–solvent interaction and the entropic costs arising from local chain confinement of polymer strands, resulting in asymmetric one- or two-patch structures. When $\chi < \chi_c$, the chain−solvent attraction increases, and the contribution of entropy gains becomes dominant which led to all three tips of Au nanoprisms simultaneously occupied by polymer strands, thereby forming symmetric three-patch structure. This scaling theory-based model effectively explained the temperature dependence of patch formation and provides a thorough understanding of the balance between entropic and enthalpic effects, which governs polymer patterning on NPs.

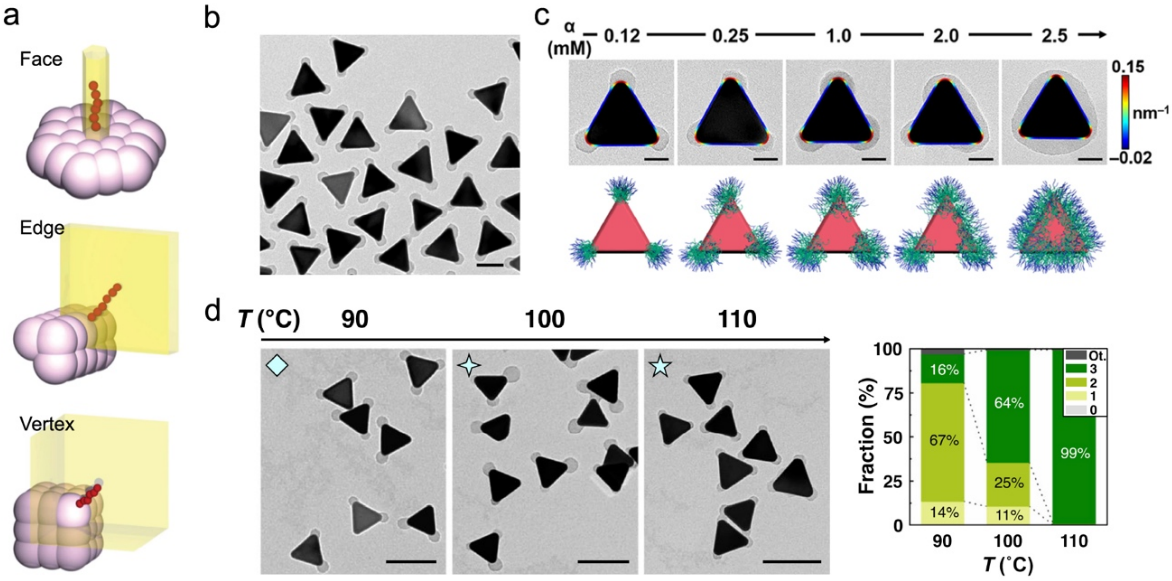

Figure 7. Site-selective ligand grafting for patch formation in NPs. (**a**) Voronoi cells for ligands grafted on the face (**top**), edge (**middle**), and vertex (**bottom**). (**b**) Representative TEM images of symmetric tip-patched Au nanoprisms. (**c**) TEM images and the corresponding schematics of patchy Au nanoprisms synthesized at increasing α (defined as the ratio of ligand molar concentration to optical density of the Au nanoprism suspension at its maximum extinction wavelength). (**d**) TEM images and histograms of patchy Au nanoprisms with the different n, synthesized at varying reaction temperature (α = 50 nM). Scale bars: (**b**) 50 nm, (**c**) 20 nm, and (**d**) 100 nm. (**a**) Reproduced with permission from ref. [49]. Copyright 2012, The Royal Society of Chemistry. (**b**,**c**) Reproduced with permission from ref. [50]. Copyright 2019, American Chemical Society. (**d**) Reproduced with permission from ref. [51]. Copyright 2022, Springer Nature.

In order to generalize such studies of patch formation, Chen and coworkers further advanced automatic TEM images by involving the machine learning (ML)-based convolutional neural networks to analyze patch shapes on Au nanoprisms [52]. A pixel in the TEM image was classified as a non-overlaying part of a NP (Channel 1), an overlaying part of NPs (Channel 2), and the background (Channel 3) by a trained U-net with three output channels. The three-channel U-Net predicted both the Au core and patches at pixel-wise accuracy as high as 99.5% (Figure 8a). Additionally, based on the shape fingerprints, described as $d(\theta)$ (defined in Figure 8b) of both the Au cores and patches, the patch shapes were classified into six groups using the Gaussian mixture model (GMM) after principal component analysis. The GMM-based classification was carried out based on patch coverage (defined as the angular range θ of the Au core covered by a polymer patch) and the symmetricity of individual patches relative to the Au nanoprism tip (Figure 8c,d). Consequently, the ML-based TEM image analysis statistically demonstrated patch coverage increased with α, which is consistent with their previous work (Figure 8e,f) [50].

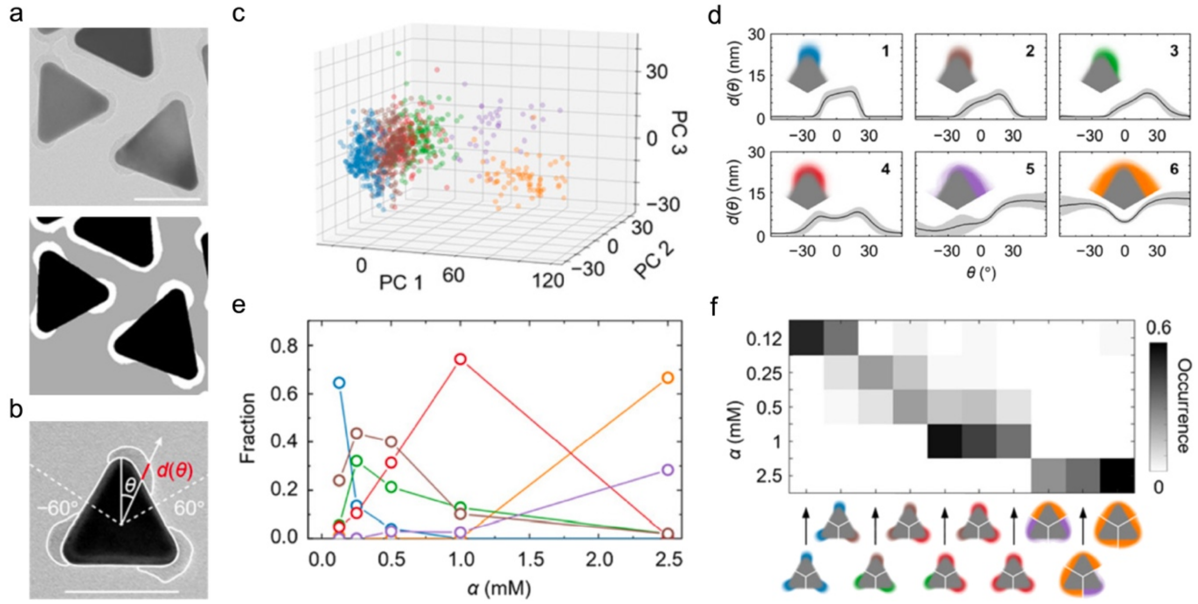

Figure 8. ML-based image analysis of polymer-grafted Au nanoprisms. (**a**) TEM image of tip-patched Au nanoprisms (**top**) and the corresponding predicted image (**bottom**), obtained by a trained three-channel U-Net. The black, white, and gray colors indicate Au core, polymer patch, and the background, respectively. (**b**) TEM image overlaid with shape contours and the shape fingerprint. $d(\theta)$ corresponds to the length of the red segment. (**c**) Shape fingerprints projected onto the first three principal components, with each color denoting a shape group predicted by the GMM. (**d**) Averaged shape fingerprint for each group predicted by GMM. Patch coverage increases from groups 1 to 6. The fingerprints of groups 1, 4, and 6 show symmetric patch distributions around $\theta = 0°$, while those of groups 2, 3, and 5 exhibit asymmetric patch distributions. The colors of patches correspond to those of the data points in (**c**). (**e**) Fractions of each GMM group as a function of α. (**f**) Occurrence of patch combinations within a Au nanoprism at different α. Scale bars: (a,b) 50 nm. Reproduced with permission from ref. [52]. Copyright 2022, The Royal Society of Chemistry.

2.6. Other Synthesis Methods for Patchy NPs

Besides the wet chemistry synthesis methods discussed above, there have been efforts combining top-down microfabrication with wet chemistry methods to synthesize patchy Au NPs. Félidj and coworkers achieved patches on the lithographically deposited Au nanodisks by using plasmon-driven reduction of aryl diazonium salts [53]. Aryl radicals, formed by reducing diazonium salt, covalently bound to the Au NP surface, followed by a successive polymerization of aryl radicals on the grafted layers. This reaction only occurs on the exposed top side of the nanodisks, with the other side in contact with substrate uncoated. The polyaryl patch thickness could be controlled from monolayers to multilayers, up to tens of nanometers, by adjusting the laser wavelength and incident polarization. Importantly, the reaction does not occur uniformly on the exposed side of nanodisk but selectively at regions where the local electric field was enhanced due to the excited multipolar plasmon modes. As a result, the polyaryl layers are most dense at the tips, lateral sides, and the apexes, with slight deposition on the edges of the nanodisks under dipolar, quadrupolar, and sextupolar excitations, respectively (Figure 9a,b). In this example, the substrate for the deposited nanodisks served as physical protection to ensure only one side of the nanodisk is exposed to reactants, and then the plasmonic modes determine the lateral distribution of the patches.

Similarly, other templates can be used to selectively coat Au NPs with polymer patches. For example, templated methods have been used for synthesizing patchy micron-sized particles by applying coating techniques, such as atomic layer deposition to embed the particles on substrates [14–16]. He and coworkers reported a templated method for creating patches on NPs [54]. Citrate-stabilized Au NPs were first adsorbed onto positively charged silica microspheres through electrostatic attraction. The exposed surfaces of NPs were modified with poly(N-isopropylacrylamide) (PNIPAM), followed by dissolution of the microsphere templates, resulting in Janus Au NPs (Figure 9c–e). These templated methods described above can strictly limit the regions where polymer is grafted onto the Au NP surface, ensuring that the original surface properties of the core NPs remain intact. This advantage potentially enables exploitation of the unaltered surface chemical properties of Au, such as its capability to form versatile chemical bonds (e.g., Au–thiol, Au–amine, and Au–catechol bonds) with additional ligands, thereby facilitating the formation of multifunctional patchy Au NPs with different types of polymer patches on surfaces.

Lastly, in situ polymerization of monomers onto Au NPs can be used for the synthesis of polymer patches [55,56]. Xia and coworkers modified the PS precipitation polymerization process by adding Au NPs. When citrate-capped Au NPs were introduced after the onset of PS polymerization, asymmetric Janus Au–PS NPs were formed (Figure 9f). PS bumps initially formed on the Au NP surface through heterogeneous nucleation, followed by polymerization on the "nuclei", which resulted in monodisperse Janus structures (Figure 9g). Interestingly, aggregates of multiple Au NPs were contained in the PS patches when the Au NPs were introduced before the onset of polymerization, while "core-free" structures, as well as Janus NPs, formed when the Au NPs were added 30 min after the polymerization was initiated. This observation indicates that the timing of Au NP addition is critical for determining the NP stability during synthesis, suggesting that PS oligomers formed in the early stage of polymerization and possibly stabilized the Au NPs during the patchy NP formation [55]. Furthermore, it was also demonstrated that various core NPs, such as Pt and Pd NPs, can be utilized for the synthesis of Janus NP [56]. This in situ polymerization method is expected to work for as long as the initially formed oligomers can exhibit sufficient attraction to the core NP surface. Therefore, this method potentially expands libraires of patchy NP compositions for both core NPs and polymer patches by fine tuning the surface chemistry of the core NPs, thereby inducing polymer–NP interactions and creating diverse patchy NPs.

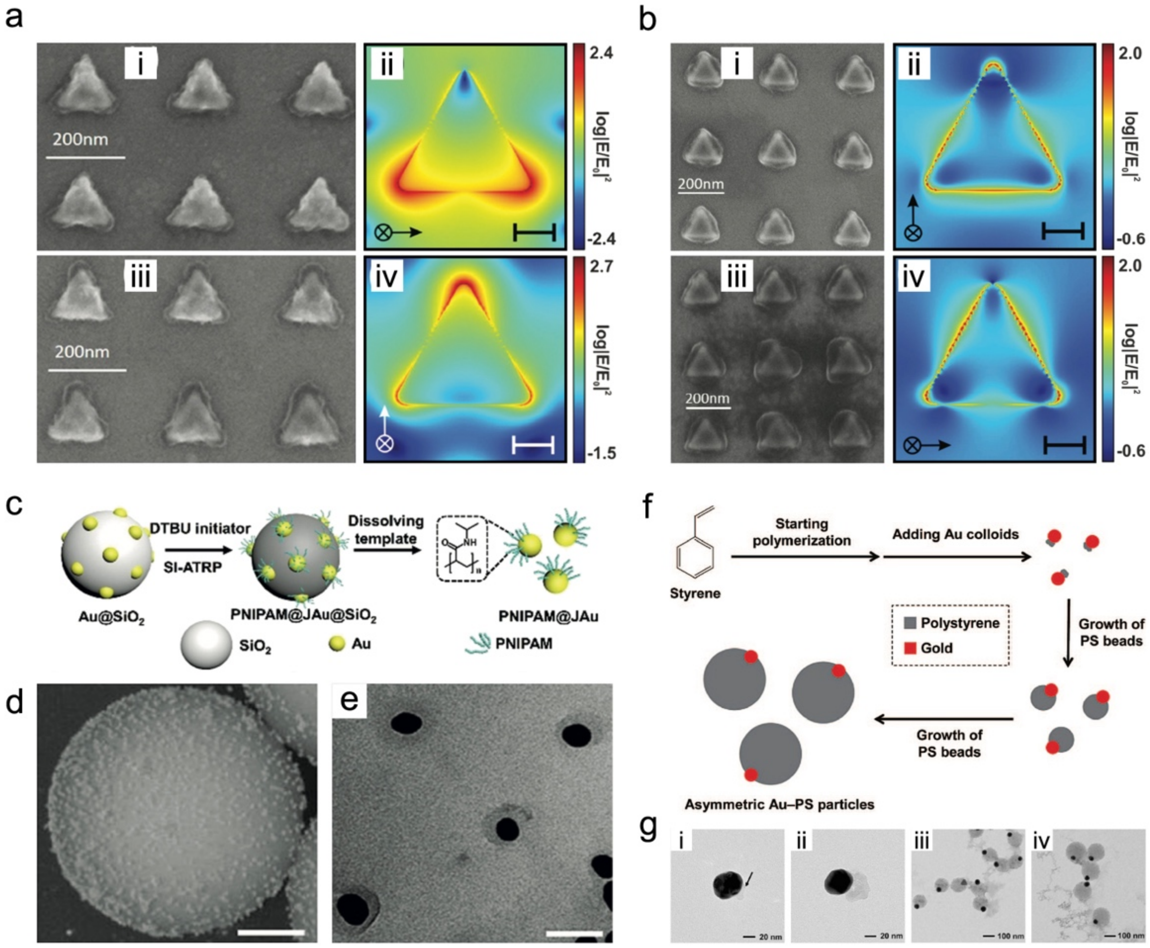

Figure 9. Other methods for the synthesis of patchy Au NPs. (**a**,**b**) SEM images of patchy Au NPs synthesized through a plasmon-induced grafting of polymers with polarization along two different directions (**left**), and the corresponding mapping of the electric field intensity (**right**) under dipolar (**a**) and quadrupolar (**b**) modes. The arrows in the electric field intensity maps indicate the polarization axis. (**c**) Schematic of a templated method for Janus Au NP synthesis. (**d**) SEM image of Au NPs adsorbed on a silica microparticle template. (**e**) TEM image of Janus Au NPs with PNIPAM patches synthesized via a templated method. (**f**) Schematic illustrating the synthesis procedure of Au–PS Janus NPs through the in situ polymerization method. (**g**) TEM images showing the morphology evolution of Au–PS Janus NPs collected at 5 min (black arrow indicates the heterogeneously polymerized PS shell), 10 min, 30 min, and 45 min during synthesis (from left to right). Scale bars: (**a**,**b**) 50 nm, (**d**) 500 nm, and (**e**) 50 nm. (**a**,**b**) Reproduced with permission from ref. [53]. Copyright 2021, The Royal Society of Chemistry. (**c**–**e**) Reproduced with permission from ref. [54]. Copyright 2019, Wiley-VCH. (**f**,**g**) Reproduced with permission from ref. [55]. Copyright 2009, American Chemical Society.

3. Self-Assembly of Patchy NPs

Patchy NPs consist of two types of surfaces—partially exposed core NP surface and polymer patch region—which exhibit different chemical and/or physical properties. This surface heterogeneity of patchy NPs enables the design of complex and programmable assemblies with controlled orientations of building blocks through directional inter-NP interactions. These inter-NP interactions occur in various forms such as van der Waals attraction, electrostatic repulsion, and steric hindrance. This section provides a detailed discussion of diverse strategies for the self-assembly of patchy NPs, categorized into parts based on if the patches are mutually attractive or repulsive. Note that because current synthesis of NPs is not large quantity yet with high uniformity, crystalline assembly of patchy NPs into superlattices has not been achieved yet. The achieved assemblies are limited to small-sized disordered clusters that are composed of fewer than 20 NPs.

3.1. Assembly of Patchy NPs Following Patch−Patch Attractions

Polymer patches on the core NPs can serve as attractive sites, inducing patch−patch attraction for assembly of loosely packed structures. Kumacheva and coworkers first reported a method for assembling tip-patched Au NRs, synthesized using site-selective adsorption of HS-PS ligands to the high curvature ends of Au NRs, by reducing the solvent quality [57]. Solvent quality was intentionally reduced by adding water to create a poor solvent environment for PS blocks. This caused the polymer patches of neighboring Au NRs to connect with each other to minimize the polymer−solvent interfaces. The resulting assembly structures were finely controlled, ranging from rings and chains to side-to-side segregated bundles of chains and spheres, as well as tip-to-tip connected bundles of chains. These structures were determined by solvent types and water fraction, which govern the quality of the solvent mixture. The change in LSPR was observed differently depending on the assembly shape and distance of Au NRs. As the distance between NRs in the end-to-end assembly increased, the longitudinal plasmon mode underwent a significant blue shift due to the decreasing plasmonic coupling. Additionally, variation in the separation between the metal blocks, resulted from controlling the water fraction, also resulted in a shift of the plasmonic band. Following this method, solvent quality-mediated assembly has been applied to various shaped NPs, such as Au NCs, Au NSs, and Ag nanoprisms, leading to diverse loosely packed clusters that cannot be assembled from non-patchy NPs [27].

He and coworkers also demonstrated heat-induced patch−patch attraction for controlled assemblies using dumbbell-like patchy Au NRs synthesized with a polymer ligand mixture (HS-PS) and PS-*b*-PEO [37]. While patchy Au NRs remained stable in solution at room temperature, the dynamics of block copolymers significantly increased at elevated temperatures of 90 °C. At this temperature, polymer solubility is enhanced, resulting in the destabilization of patches on the core Au NR and partial desorption of polymer strands due to weakened hydrophobic interactions between the ligands and polymers. After the desorption of the polymer strands from the Au NR surface, the exposed PS ligands became thermodynamically unfavorable, prompting end-to-end assembly of Au NRs, thereby the formation of chain-like structures to minimize the interfacial area between NR and solvent (Figure 10a). Notably, the formation of end-to-end assemblies between Au NRs was also confirmed by monitoring changes in LSPR. After 1.5 min from the onset of Au NR self-assembly, the UV–vis spectrum exhibited a distinct peak at 805 nm, attributed to plasmonic coupling in short NR chains. As the thermal annealing time increased, the LSPR red-shifted to 830 nm due to the elongation of the chains (Figure 10b). Lastly, since NP−solvent interfacial energy is a key parameter governing the assembly process, the water fraction, which determines solvent quality, also influenced the kinetics of the assembly process (Figure 10c).

When patches are charged, patch−patch attractions can be triggered by complexation of polymer patches and molecular additives. “Bridge” molecules or ions of an opposite charge to the patches can induce self-aggregation between charged polymer patches. For instance, Cu_2^{4+} and Co^{2+} were shown to induce complexation of block copolymer patches on Au NPs containing acrylic acid group, such as P(4VPA) [34] and PAA [38] segments, resulting in assemblies such as elongated chain-like structures (Figure 11a) and clusters (Figure 11b) via patch−patch agglomeration.

Beyond multivalent ions, ionic surfactants can also induce the complexations of charged patches. Chen and coworkers demonstrated complexation of patches by introducing CTAB, a cationic surfactant, into a tip-patched Au nanoprism system, synthesized with thiol-terminated ligands and physisorbed PS-*b*-PAA [51,58]. The patchy Au nanoprisms were suspended in water, with the PAA blocks protruding towards water. The head group of CTAB electrostatically bound to the negatively charged PAA blocks, followed by hydrophobic attractions among the tails, leading to the aggregation of polymeric patches (Figure 11c–f). This CTAB-induced complexation of tip-patchy prisms resulted in diverse assembly structures such as linear, cyclic, and branched chains. The assembled trimer exhibited symmetric bonding (2.25 eV) and anti-symmetric antibonding (2.29 eV) modes, depending on the excitation energy, due to the plasmonic coupling effect (Figure 11g).

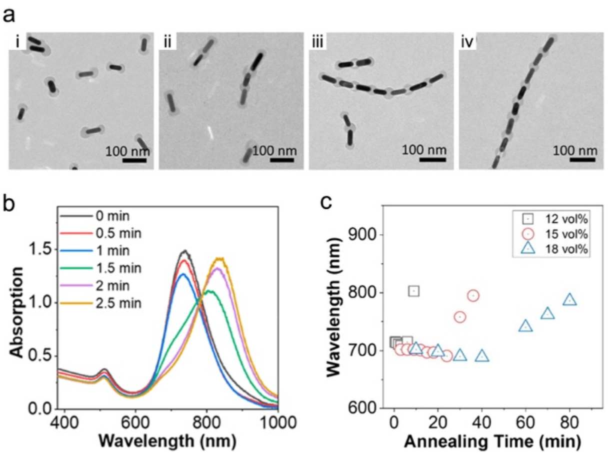

Figure 10. Assembly of patchy Au NPs via patch−patch attractions. (**a**) Representative TEM images of patchy Au NRs at increasing thermal annealing times (from **left** to **right**). (**b**) UV−vis spectra of the self-assemblies at different time points. (**c**) The longitudinal plasmon band of patchy Au NRs during thermal treatment at different water volume fractions as a function of annealing time. Reproduced with permission from ref. [37]. Copyright 2023, American Chemical Society.

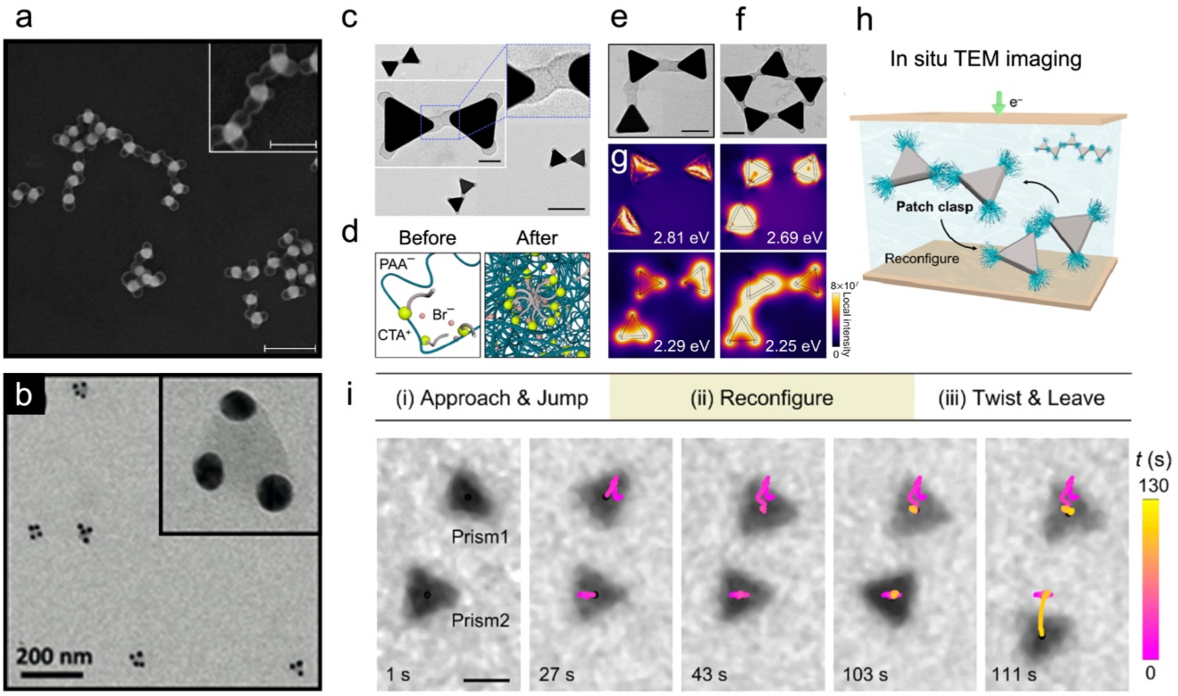

Figure 11. Assembly of patchy Au NPs via patch−patch attractions induced by complexation between polymeric patch and additive moieties. (**a**,**b**) Self-assembly of patchy Au NPs driven by multivalent cations, forming small clusters and elongated chain-like structures. (**c**) TEM image of patchy Au nanoprism dimers. (**d**) Schematics illustrating CTAB and PAA blocks before (**left**) and after (**right**) complexation. (**e**,**f**) TEM images of a Au nanoprism trimer (**e**) and multimer (**f**) created through CTAB-induced complexation. (**g**) The spatial electric field distribution maps of the trimer in (**e**) at different excitation energies. (**h**) Schematic illustrating the self-assembly of patchy Au nanoprisms into a dimer in a liquid chamber for in situ TEM imaging. (**i**) Time-lapse liquid-phase TEM images for the assembly and disassembly of patchy Au nanoprisms. Scale bars: (**a**) 200 nm (inset: 100 nm), (**c**) 200 nm (inset: 20 nm), and (**e**,**f**,**i**) 50 nm. (**a**) Reproduced with permission from ref. [38]. Copyright 2021, American Chemical Society. (**b**) Reproduced with permission from ref. [34]. Copyright 2019, Wiley-VCH. (**c**,**d**,**f**,**h**,**i**) Reproduced with permission from ref. [58]. Copyright 2024, American Chemical Society. (**e**,**g**) Reproduced with permission from ref. [51]. Copyright 2022, Springer Nature.

Such complexation induced self-assembly is often considered as a “soft” bond that is flexible and dynamic. The assembly and disassembly dynamics of the patchy Au nanoprisms discussed above was investigated using liquid-phase TEM in real-time (Figure 11h) at low dose rate to minimize the electron beam damage [58]. At the beginning of patch−patch assembly, patchy Au nanoprisms approached each other by slow crawling, followed by a sudden jump, forming a tip-to-tip assembly. The assembled dimer of the patchy Au nanoprisms then maintained a stable center-to-center distance, indicating a robust longitudinal connection between the patch Au NPs. Meanwhile, each NP exhibited rotational flexibility with a fluctuating tip–tip angle, which was attributed to the dynamic reorganization of polymer chains while maintaining the associations in the linked patches, referred to as the “patch clasping”. Finally, when disassembly happened, the NPs twisted against each other, eventually breaking apart into two individual patchy Au nanoprisms (Figure 11i), showing the reversibility of the self-assembly process.

These soft “bridges” linking patchy NPs do not strictly restrict the direction of the bonds in assembly, allowing rotational distortion of the structures without breaking any bonds, and can serve as emerging mechanical metamaterials. Meanwhile, when this patch−patch assembly occurs, complexation of patches proceeds rapidly, not allowing enough time to find the configurations that is thermodynamically most stable, resulting in assembly in cluster-scale consisting of a small number of NPs with low structural crystallinity.

3.2. Assembly Involving Mutually Repulsive Patches

When the patches are repulsive, they can assemble driven by the van der Waals attractions of the core NPs. Chen and coworkers first reported the self-assembly of Janus Au NPs via salt-induced agglomeration, where the electrostatic repulsion between negatively charged PAA blocks of the polymer patches was screened by adding sodium chloride. The weakened repulsion allows the Au NPs to aggregate through van der Waals attraction, preferentially along the uncoated Au surfaces (Figure 12a) [41]. Following this study, Nie and coworkers also utilized salt-induced surface charge screening to assemble other patchy Au NPs with negatively charged patches, leading to petal-like clusters of Janus Au NSs (Figure 12b) [38]. The balance of the electrostatic repulsion of patches and van der Waals attraction between Au has been discussed using the Derjaguin-Landau-Verwey-Overbeek theory [59,60]. The limitation of this method is the relative low level of control in the assembly yield, especially for shape anisotropic NPs where many relative configurations are possible. For example, in the case of tip-patched Au nanoprisms, both star- and slanting diamond-shaped assemblies of tip-patched Au nanoprisms (Figure 12c,d) [50] were formed spontaneously in the same system with very similar levels of free energy.

In addition to ionic additives, solvent variations can also control the surface charge of patchy NPs and induce assembly [36]. He and coworkers synthesized Janus Au NPs with neutral PS-*b*-PEO block copolymers. These NPs were stabilized in water due to both the steric hindrance of polymer patches and the electrostatic repulsion from charges on the polymer-free Au surface originated from CTAB surfactant out of Au NP synthesis. When ethanol was introduced into this Janus Au NP dispersion, selective removal of CTAB was achieved due to its high solubility in ethanol, decreasing the surface charge on Au NPs. This decrease led to the aggregation of patchy Au NPs along the exposed Au surface through Au–Au van der Waals attractions (Figure 12e), while steric patch−patch repulsion was maintained.

Going beyond the generic van der Waals attraction of core NPs, other more specific attractions can be used to counteract with mutually repulsive patches and to induce self-assembly. One of such specific attraction is DNA hybridization. Broadly, Au NPs capped with single-stranded DNAs (ssDNAs) have been studied as building blocks for assemblies since they readily form hydrogen bonds with complementary strands [61–64]. Therefore, the use of ssDNAs, as additional linkers, have also been explored for the assembly of patchy NPs. Lu and coworkers utilized Janus NSs for this DNA hybridization-driven assembly [65]. After synthesizing patches with PS-*b*-PAA on Au NSs, the uncoated Au surfaces were functionalized with thiol-terminated ssDNAs (Figure 12f). These post-functionalized Janus particles were assembled with other NPs (either bare or patchy Au NPs) coated with complementary ssDNAs (Figure 12g,h), or linker strands consisting of the complementary sequence (Figure 12i). In addition to NSs, differently shaped patchy NPs, such as Au NRs and nanoprisms, were also utilized for this complementary DNA-induced assembly, leading to a wide library of assemblies, ranging from small clusters to large chain-like structures [42].

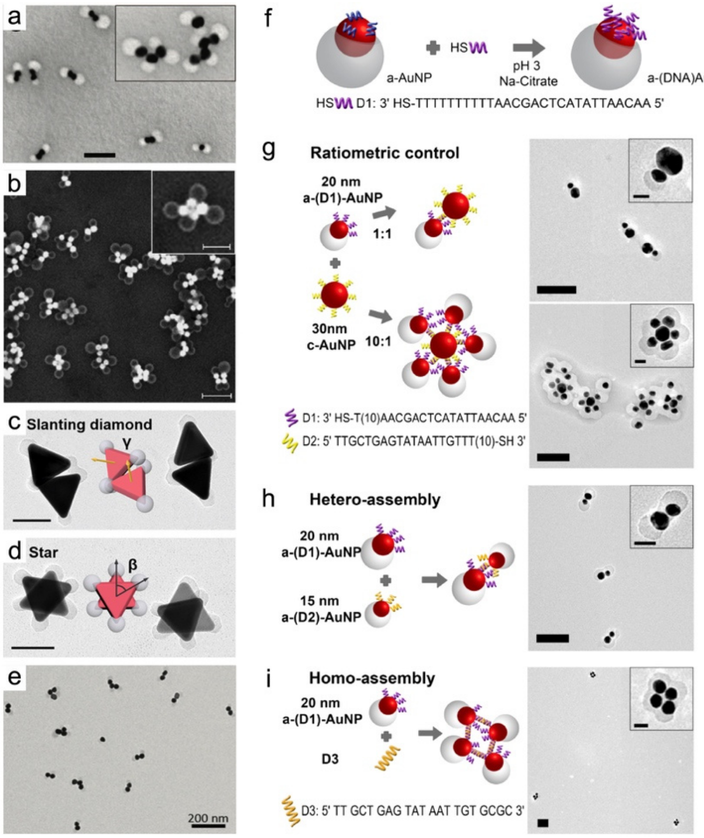

Figure 12. Assembly of patchy Au NPs in the presence of mutually repulsive patches. (**a**,**b**) TEM and SEM images of Janus Au NP assemblies induced by screening the surface charge of the patches using sodium chloride. (**c**,**d**) TEM and SEM images of self-assemblies of patchy Au nanoprisms exhibiting slanting diamond- (**c**) and star-like (**d**) shapes. (**e**) TEM images of Janus Au NP clusters assembled upon the addition of ethanol. (**f**) Schematic illustrating the functionalization of Janus Au NPs with ssDNAs. (**g**) Schematic and TEM images of assemblies of Janus Au NSs and bare NPs functionalized with complimentary ssDNAs. The structures of clusters can be controlled by the ratios of the two building blocks. (**h**,**i**) Schematic and TEM images of hetero-assembly between differently sized Janus Au NSs (**h**), and homo-assembly of Janus Au NSs using linker ssDNA strands (**i**). Scale bars: (**a**) 100 nm, (**b**) 200 nm (inset: 100 nm), (**c**,**d**) 50 nm, and (**g–i**) 100 nm (insets: 25 nm). (**a**) Reproduced with permission from ref. [41]. Copyright 2008, American Chemical Society. (**b**) Reproduced with permission from ref. [38]. Copyright 2021, American Chemical Society. (**c**,**d**) Reproduced with permission from ref. [50]. Copyright 2019, American Chemical Society. (**e**) Reproduced with permission from ref. [36]. Copyright 2022, The Royal Society of Chemistry. (**f–i**) Reproduced with permission from ref. [65]. Copyright 2013, American Chemical Society.

4. Applications of Patchy Plasmonic NPs

Polymer-patched plasmonic NPs are expected to be useful in various application fields due to their spatially heterogeneous and hybrid chemical, physical, and geometrical surface features. Thus efforts on applications have been emerging despite the short history of research on patchy NPs. This section highlights two applications of patchy NPs: one is the use of templates for overgrowth of complex NPs, and the other is self-propelling nanomotors.

4.1. Templates for Overgrowth

The surface heterogeneity of patchy NPs imparts different chemical reactivities for polymer patches and uncoated NP surfaces, enabling their use as unique templates for subsequent reaction via seed-mediated growth. Wang and coworkers demonstrated the site-selective deposition of metals on the uncoated Au surface of patchy Au NPs as the PS-*b*-PAA polymer patches blocked the diffusion of the reactants into contact with the core NPs [46]. A metal precursor and a mild reducing reagent (hydroquinone) were introduced into the patchy Au NP dispersion, followed by overnight overgrowth to facilitate further deposition. This process resulted in two distinct domains—overgrown metal layer and polymer patch regions—on the core Au NP surfaces. The deposition on patchy Au NPs was effective regardless of the polymer patterns and core NP shapes including rods, bipyramids, and triangular prims (Figure 13a). Furthermore, a multi-step overgrowth reaction was also demonstrated. After the initial overgrowth of Pd on both ends of patchy Au NRs, with a polymer patch in the middle, additional heating-induced transformation was performed, thereby leading to further contraction of the polymer patches. This process created small gaps between Pd (at both ends) and polymer patch (in the middle), where additional Ag can be selectively deposited. Through this multi-step metal deposition, Au NRs with three distinct surface domains—Pd, Ag, and polymer patch—were synthesized (Figure 13b–d). It should be noted that these new metallic domains can be also used for further surface functionalization, which can be easily carried out using sulfide reagents. The applicability of patchy Au NP as templates was further demonstrated through the overgrowth of silica domains using silane coupling reagents (tetraethyl orthosilicate) beyond metals (Figure 13e) [47], and the patchy NP assemblies beyond discrete NPs (Figure 13f,g) [37].

It was also demonstrated that multi-component plasmonic NPs can be synthesized by selectively removing polymer patches from patchy NPs with overgrown domains. Xia and coworkers first synthesized Au–PS Janus NPs through the in situ polymerization method (discussed in Section 2.6), followed by the deposition of Ag onto the Au NPs [66]. The PS patches were then selectively removed using organic solution (tetrahydrofuran containing PVP and ethanol), resulting in Au–Ag Janus NPs (Figure 13h–j). Similarly, since different metallic compositions (Pd and Pt) can be utilized for overgrowth on Au–PS Janus NPs, similar Au–Pd (Figure 13k,l) and Au–Pt (Figure 13m,n) Janus NPs were also synthesized by selective removal of PS patches. Lastly, asymmetric, bowl-like NPs were also achieved by etching of polymer patches from the Janus Au NCs with overgrown metal (Au, Ag, and Pd) domains (Figure 13o) [67].

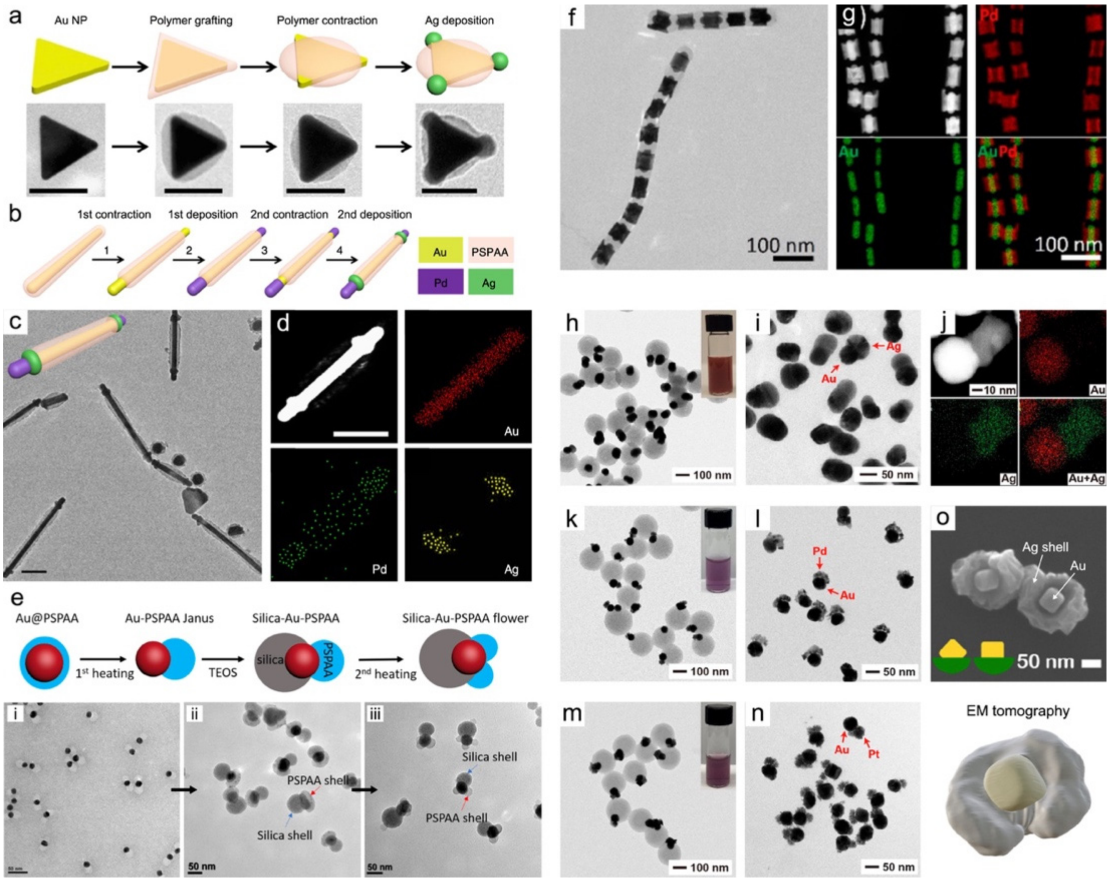

Figure 13. Patchy Au NPs as templates for overgrowth. (**a**) Schematics and TEM images illustrating the overgrowth of Ag on PS-*b*-PAA patchy Au nanoprisms. (**b–d**) Schematics (**b**), TEM image (**c**), and energy dispersive X-ray (EDX) mapping (**d**) of patchy Au NRs subsequently deposited with Pd and Ag via multi-step overgrowth. (**e**) Schematics and TEM images of silica-overgrown Janus Au NPs. (**f**) TEM and (**g**) EDX mapping of chain-like assemblies of patchy Au NRs after Pd-overgrowth. (**h**) TEM images of Au−PS Janus NPs after Ag overgrowth. (**i**) TEM and (**j**) EDX mapping of Au−Ag Janus NPs after selective removal of PS patch. (**k,l**) TEM images of Pd-overgrown Au−PS Janus NPs before (**k**) and after (**l**) selective removal of PS patch. (**m,n**) TEM images of Pt-overgrown Au−PS Janus NPs before (**m**) and after (**n**) selective removal of PS patch. The top-right insets in (**h**), (**k**), and (**m**) show Au−PS Janus NP solutions after metal overgrowth. (**o**) SEM image (top) and EM tomography (bottom) of Au−Ag bowl-like NPs after selective removal of PS-*b*-PAA patch. Scale bars: (**a**) 50 nm and (**c**,**d**) 100 nm. (**a–d**) Reproduced with permission from ref. [46]. Copyright 2018, Springer Nature. (**e**) Reproduced with permission from ref. [47]. Copyright 2019, American Chemical Society. (**f**,**g**) Reproduced with permission from

ref. [37]. Copyright 2023, American Chemical Society. (**h–n**) Reproduced with permission from ref. [66]. Copyright 2019, American Chemical Society. (**o**) Reproduced with permission from ref. [67]. Copyright 2022, The Royal Society of Chemistry.

Furthermore, Nie and coworkers also reported overgrowth of additional composition on patchy Au NPs [68]. The end-grafted patchy Au NRs were first synthesized with HS-PS, based on the high curvature preference of ligand grafting. Then, end-to-end self-assembly was induced by the reducing solvent quality, followed by the introduction of various precursors along with a mild reducing reagent (L-ascorbic acid), which resulted in the overgrowth of different components on the exposed Au surfaces (Figure 14a,b). This overgrown chain-like structure can be dissociated by increasing the solvent quality again, leading to individual coaxial NPs with multiple domains—Au surfaces and overgrown shells. The thickness of the overgrown shell was finely tuned by controlling the amount of precursor, thereby enabling coaxial multi-domain NPs with controlled shell thickness (Figure 14c). Importantly, various compositions can be utilized to form the overgrown shell, including not only pure metals (Pt and Ag) but also metal oxides (Cu_2O and CeO_2) (Figure 14d,e).

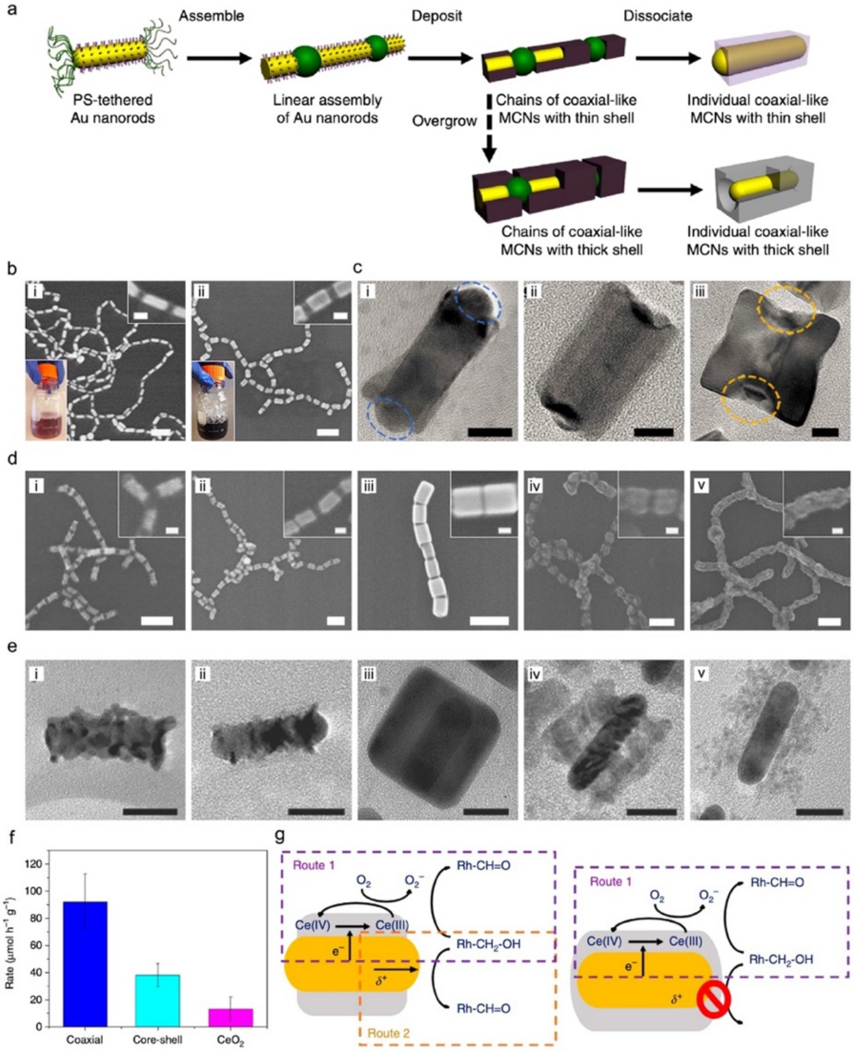

Figure 14. Patchy Au NRs as templates for overgrowth of various components and their catalytic applications. (**a**) Schematic illustrating the overgrowth on chain-like assemblies of patchy Au NRs and their subsequent dissociation into individual coaxial multi-domain NPs. (**b**) High- and low-magnification SEM images of patchy Au NR chains before (**left**) and after (**right**) Pd overgrowth. The bottom-left insets show product solutions with a visible color change upon Pd deposition. (**c**) High-resolution TEM images of individual coaxial multidomain NPs after the dissociation of Pd-overgrown chain-like patchy NR assemblies, showing increase in shell thickness (from **left** to **right**). Blue and yellow circles indicate exposed Au NR and cavities at the tips, respectively. (**d**) SEM and (**e**) high-resolution TEM images of chain-like patchy Au NR assemblies after overgrowth of Pt, Pt/Ni, Ag, Cu_2O, and CeO_2 (from **left** to **right**). (**f**) Rate of benzaldehyde generation for coaxial multi-domain and core–shell of Au–CeO_2, as well as pure CeO_2 NPs. (**g**) Schematics illustrating the proposed photo-oxidation mechanisms for coaxial multi-

domain (**left**) and core–shell (**right**) Au–CeO_2. Scale bars: (**b**) 100 nm (insets: 20 nm), (**c**) 10 nm, (**d**) 100 nm (insets: 20 nm), (**e**) 20 nm. Reproduced with permission from ref. [68]. Copyright 2016, Springer Nature.

These individual multi-domain NPs can be used for photocatalysis. The Au–CeO_2 coaxial multi-domain NPs exhibited effective photo-oxidization ability of transforming benzyl alcohol to benzaldehyde. Compared to core–shell Au–CeO_2 structure and pure CeO_2 NPs, the coaxial multi-domain NPs effectively catalyzed this benzyl alcohol transformation (Figure 14f). This improved catalytic effect can be attributed to the efficient utilization of photogenerated charge carriers (hot electrons and holes), facilitated by the exposure of CeO_2 shells and Au cores. When using coaxial multi-domain NPs, two reaction pathways can contribute to benzaldehyde generation. First, photogenerated hot electrons are injected from Au core to CeO_2, which reduces Ce(IV) to Ce(III). The Ce(III) species react with dissolved oxygen in solution and generate superoxides, which oxidize benzyl alcohol. Second, positive charges accumulated on Au cores can directly oxidize benzyl alcohol on the exposed Au NR tips, while the core–shell can exploit the first pathway only due to the absence of the exposed Au surfaces (Figure 14g). Thus, through the synergistic effect of these two pathways, the coaxial multi-domain NPs effectively oxidized benzyl alcohol, demonstrating the improved catalytic performance.

4.2. Self-Propelling Nanomotors

Plasmonic NPs with a symmetry-broken shapes can also exhibit self-propulsion capability as they have site-dependent reactivity to surrounding chemical reagents [21]. He and coworkers demonstrated the use of Janus Au NPs, synthesized by a templated method (discussed in Section 2.6) for self-propulsion. Glucose oxidase was covalently bound to the exposed Au surface of Janus Au NPs. This chemical enzyme enabled the reduction of glucose in solution, creating local gradients of glucose, gluconic acid, and H_2O_2 across the NP, which can drive self-propulsion (Figure 15a) [54]. The chemotactic behavior of the symmetry-broken Janus Au NPs was investigated in microfluidic channels with concentration gradient of glucose fuel (Figure 15b). The Janus Au NPs in the reservoir with a low glucose concentration readily moved toward the high-glucose concentration region over time (Figure 15c,d), which indicates their self-propulsion capability.

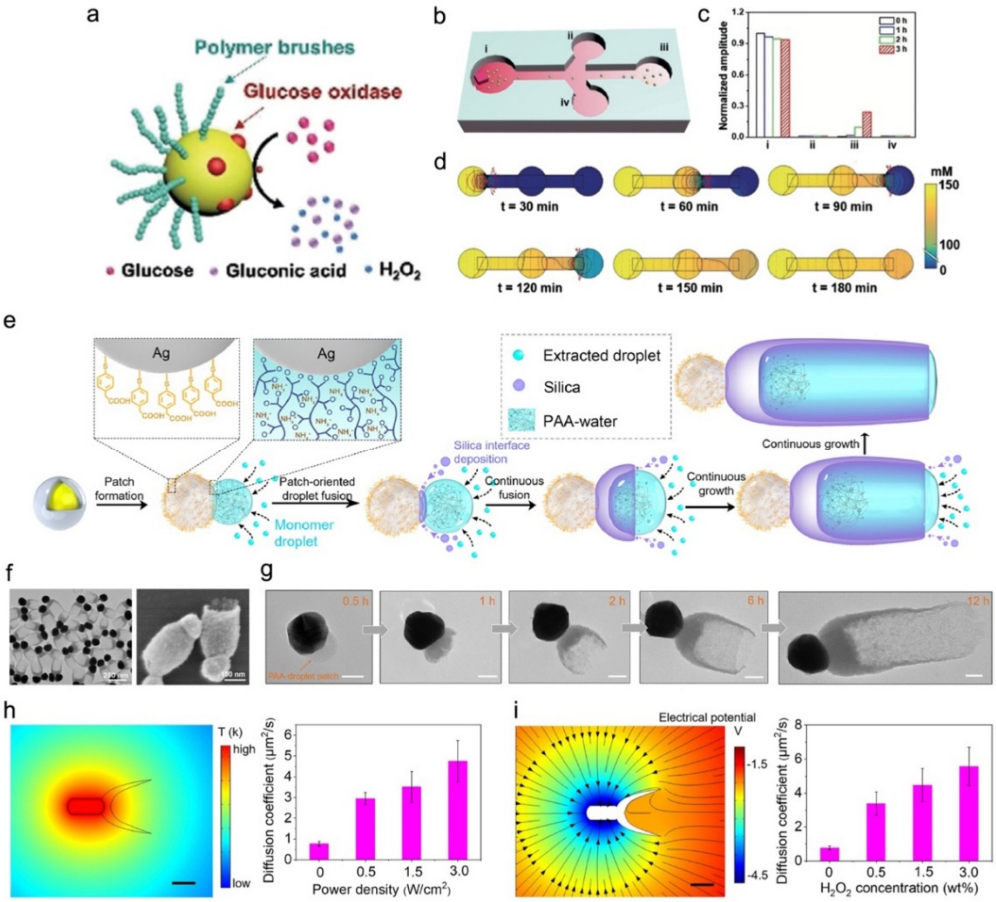

Figure 15. Patchy plasmonic NPs as self-propelling nanomotors. (**a**) Schematic of the motion of glucose oxidase-decorated Janus Au NSs in glucose solutions. (**b**) Schematic of the chemotaxis of the Janus Au NPs towards in a

microfluidic channel with a glucose concentration gradient. After introducing Janus Au NPs into the left reservoir (i), a piece of agarose gel containing glucose was placed in the right reservoir (iii) to make a horizontal glucose concentration gradient. (**c**) Absorbance changes of Janus Au NPs at different time points after the initiation of self-propelling motion. (**d**) Computational simulation showing the diffusion profile of glucose in the microfluidic channel at different time intervals. (**e**) Schematic illustrating the formation of Janus Au@Ag core−shell NPs through directional growth of a hollow silica shell, along with TEM (**left**) and SEM (**right**) images of resulting Janus Au@Ag NPs. (**g**) TEM images showing the morphology evolution of Janus Au@Ag NPs collected at different time points during the synthesis. (**h**) Theoretically calculated steady-state temperature distribution around a Janus Au@Ag NR under 3 W/cm^2 NIR irradiation (**left**), and apparent diffusion coefficients under different laser power densities (right). (**i**) Theoretical calculation of the electric potential (color-coded) distribution and electric field (black arrows) around a Janus Au@Ag NR (**left**), and apparent diffusion coefficients at different H_2O_2 concentrations (right). Scale bars: (**g**) 50 nm and (**h**,**i**) 100 nm. (**a–d**) Reproduced with permission from ref. [54]. Copyright 2019, Wiley-VCH. (**e–i**) Reproduced with permission from ref. [69]. Copyright 2022, American Chemical Society.

Lastly, beyond polymer-patched NPs, Janus NPs with hollow silica patches were also utilized for self-propelling nanomotors. Kong and coworkers synthesized silica patches on Au-core and Ag-shell (Au@Ag) plasmonic core−shell NPs by simultaneously growing a silica shell (Figure 15e–g) [69]. These Au@Ag NPs with structural asymmetry enabled self-propulsion through a dual-mode response to both near-infrared (NIR) irradiation, which generated heat due to photothermal effect, and the formation of H_2O_2, resulting from the Ag shell. Theoretically computed temperature distributions of the Janus Au@Ag NRs under NIR irradiation showed that heat was concentrated in the exposed Au@Ag region, creating a temperature gradient between two ends. This gradient generated thermo-osmotic flow along the outer surface of the Janus Au@Ag NRs, driving the fluid toward the hotter region and thereby propelling the patchy NRs in the direction of the silica patches via self-thermophoresis (Figure 15h). Furthermore, in the presence of H_2O_2 in solution, the outmost Ag shell either catalyzed its decomposition into water and oxygen or reacted directly with it, producing HOO^- and Ag^+ ions. Due to the significant difference in diffusivity between two ions, an inward electric field formed to maintain charge neutrality in the bulk, leading to self-diffusiophoresis-based propulsion of patchy NRs (Figure 15i). This dual-mode response of patchy Au@Ag NRs enabled their effective use as self-propelling nanomotors. Therefore, the heterogeneous surface chemistry and structural characteristic of patchy NPs make them promising candidates for nanomotors applications, with potential uses in various fields such as targeted delivery and catalysis.

5. Conclusions and Outlook

Patchy plasmonic NPs have attracted interest due to their unique chemical, physical, and geometrical surface heterogeneities, which are expected to be utilized for creating assembled structure as well as diverse practical usages. In this review, we highlight progress in the synthesis and self-assembly strategies of polymer-patched plasmonic NPs and their applications. There is still considerable room for the improvements and innovation in this area.

First, although significant efforts have been made to control the polymer patterns on core NPs, the shape controllability of patchy NPs remains limited. As discussed, while synthesis strategies can be categorized differently based on their underlying mechanism, the positions of polymer patches are mostly similar, since they are governed by only a few parameters, such as local surface curvature, across NP shapes. For example, when diverse NP with different morphologies, such as rods, cubes, triangular prism, were used, high-curvature preference of patch formation is mostly effective regardless of the NP type, resulting in high-curvature region-coated patchy NPs. Even in the case of symmetric spherical NPs, the controllability of the patch configurations, such as shape and number, remained limited. The choice of polymers for patch formation has been limited to those containing PS blocks, likely owing to their hydrophobic and crosslinking properties favoring the patch formation and their chemical and thermal stability. As the hydrophobic ligands spontaneously formed domains based on their chemical properties, this dependency of the ligand within a few candidates restricts the shape diversity of patchy NPs, thereby constraining the range of their assemblies and applications.

Second, current efforts in synthesizing patchy NPs are primarily focused on the Au NP systems utilizing Au−thiol bonds. However, NPs with different compositions exhibit distinct characteristics, such as magnetism (Fe_2O_3 and Fe_3O_4) [4,70], catalytic activity (Pd, Pt, and Cu) [1–3], quantum emission (CdSe/CdS) [71], energy storage (MnO_2) [72]. These diverse chemical compositions enable different types of bonding with various end-grafted ligands containing functional groups such as thiol [73,74], amine [75], and catechol [76]. Consequently, there is potentially huge opportunity for researchers to facilitate surface coatings on these other core NP materials.

The variations of the core NP composition can also allow the fabrication of multifunctional assemblies through the clustering of two different patchy NPs can further expand their potential applications by synergistic effects.

Third, current studies in the application of patchy NPs have primarily focused on the single NP level. However, self-assembled plasmonic NPs can exhibit distinct optical properties due to the plasmon coupling effect, which depends on inter-NP distances. These newly emerging optical properties of assembled plasmonic NPs can be utilized for potential applications in catalysis and sensing. Polymer patches on NPs can govern the assembly behavior of patchy NPs by balancing various interactions such as van der Waals attraction, electrostatic repulsion, and steric hindrance, thereby forming unique assembled structures with controlled inter-NP gaps. Therefore, studying the unique properties of patchy NP assemblies, beyond those of single NPs, enables the expansion of their potential applications.

Last, the current demonstrations of self-assembled structures of patchy NPs are mostly at the cluster level, consisting of only a few numbers of building blocks. The patchy NPs provide directional and site-specific binding with each other due to additional interactions such as electrostatic forces and steric hindrance, beyond van der Waals attractions, which arise from the surface patches. Therefore, the assembly patterns of patchy NPs, when achieved in large-scale assemblies are expected to differ from those of the bare NPs. However, current strategies for creating assemblies are still in early stage. Therefore, developing an advanced synthesis method for patchy NPs with novel surface capping ligands, along with high uniformity and synthesis yields, can be a key focus for achieving large-scale assembled structure with unique packing geometries. Furthermore, there have been significant efforts in computational ways in designing and optimizing synthesis conditions for unique shapes of plasmonic NPs and predicting their assembly structures. Therefore, in addition to experimental approaches, computational tools can be utilized to establish design rules for the synthesis and make quantitative prediction for patchy NPs based various principles. By combining these computational methods with experiments, it is anticipated that novel methods for synthesizing new patchy NPs with high shape controllability can be achieved, leading to promising candidates for further large-scale self-assemblies with unique lattices. Consequently, these advancements will broaden the applications fields of patchy NPs such as optical and mechanical metamaterials.

Author Contributions: C.K. and X.L.: conceptualization, writing-original draft preparation; J.K., Y.W., and Q.C.: writing-review and editing. All authors have read and agreed to the published version of the manuscript.

Funding: The authors are grateful for support from the U.S. National Science Foundation under Cooperative Agreement No. 2243104, “Center for Complex Particle Systems (COMPASS)” Science and Technology Center.

Data Availability Statement: Not applicable.

Conflicts of Interest: The authors declare no competing financial interest.

References

1. Dong, C.; Lian, C.; Hu, S.; Deng, Z.; Gong, J.; Li, M.; Liu, H.; Xing, M.; Zhang, J. Size-dependent activity and selectivity of carbon dioxide photocatalytic reduction over platinum nanoparticles. *Nat. Commun.* **2018**, *9*, 1252.
2. Lyu, Z.; Shang, Y.; Xia, Y. Shape-controlled synthesis of copper nanocrystals for plasmonic, biomedical, and electrocatalytic applications. *Acc. Mater. Res.* **2022**, *3*, 1137–1148.
3. Miller, M.A.; Askevold, B.; Mikula, H.; Kohler, R.H.; Pirovich, D.; Weissleder, R. Nano-palladium is a cellular catalyst for in vivo chemistry. *Nat. Commun.* **2017**, *8*, 15906.
4. Park, J.; An, K.; Hwang, Y.; Park, J.-G.; Noh, H.-J.; Kim, J.-Y.; Park, J.-H.; Hwang, N.-M.; Hyeon, T. Ultra-large-scale syntheses of monodisperse nanocrystals. *Nat. Mater.* **2004**, *3*, 891–895.
5. Murray, W.A.; Barnes, W.L. Plasmonic materials. *Adv. Mater.* **2007**, *19*, 3771–3782.
6. Zheng, J.; Cheng, X.; Zhang, H.; Bai, X.; Ai, R.; Shao, L.; Wang, J. Gold nanorods: The most versatile plasmonic nanoparticles. *Chem. Rev.* **2021**, *121*, 13342–13453.
7. Lee, H.-E.; Yang, K.D.; Yoon, S.M.; Ahn, H.-Y.; Lee, Y.Y.; Chang, H.; Jeong, D.H.; Lee, Y.-S.; Kim, M.Y.; Nam, K.T. Concave rhombic dodecahedral Au nanocatalyst with multiple high-index facets for CO_2 reduction. *ACS Nano* **2015**, *9*, 8384–8393.
8. Hang, Y.; Wang, A.; Wu, N. Plasmonic silver and gold nanoparticles: Shape-and structure-modulated plasmonic functionality for point-of-caring sensing, bio-imaging and medical therapy. *Chem. Soc. Rev.* **2024**, *53*, 2932–2971.
9. Dreaden, E.C.; Alkilany, A.M.; Huang, X.; Murphy, C.J.; El-Sayed, M.A. The golden age: Gold nanoparticles for biomedicine. *Chem. Soc. Rev.* **2012**, *41*, 2740–2779.
10. García-Lojo, D.; Núñez-Sánchez, S.; Gómez-Graña, S.; Grzelczak, M.; Pastoriza-Santos, I.; Pérez-Juste, J.; Liz-Marzán, L.M. Plasmonic supercrystals. *Acc. Chem. Res.* **2019**, *52*, 1855–1864.

11. Sönnichsen, C.; Reinhard, B.M.; Liphardt, J.; Alivisatos, A.P. A molecular ruler based on plasmon coupling of single gold and silver nanoparticles. *Nat. Biotechnol.* **2005**, *23*, 741–745.
12. Tabor, C.; Murali, R.; Mahmoud, M.; El-Sayed, M.A. On the use of plasmonic nanoparticle pairs as a plasmon ruler: The dependence of the near-field dipole plasmon coupling on nanoparticle size and shape. *J. Phys. Chem. A* **2009**, *113*, 1946–1953.
13. Kim, J.; Ou, Z.; Jones, M.R.; Song, X.; Chen, Q. Imaging the polymerization of multivalent nanoparticles in solution. *Nat. Commun.* **2017**, *8*, 761.
14. Wittmeier, A.; Leeth Holterhoff, A.; Johnson, J.; Gibbs, J.G. Rotational analysis of spherical, optically anisotropic janus particles by dynamic microscopy. *Langmuir* **2015**, *31*, 10402–10410.
15. Han, M.; Yildiz, E.; Bozuyuk, U.; Aydin, A.; Yu, Y.; Bhargava, A.; Karaz, S.; Sitti, M. Janus microparticles-based targeted and spatially-controlled piezoelectric neural stimulation via low-intensity focused ultrasound. *Nat. Commun.* **2024**, *15*, 2013.
16. Chen, Q.; Bae, S.C.; Granick, S. Directed self-assembly of a colloidal kagome lattice. *Nature* **2011**, *469*, 381–384.
17. Wang, Y.; Hollingsworth, A.D.; Yang, S.K.; Patel, S.; Pine, D.J.; Weck, M. Patchy particle self-assembly via metal coordination. *J. Am. Chem. Soc.* **2013**, *135*, 14064–14067.
18. Garbuzenko, O.B.; Winkler, J.; Tomassone, M.S.; Minko, T. Biodegradable Janus nanoparticles for local pulmonary delivery of hydrophilic and hydrophobic molecules to the lungs. *Langmuir* **2014**, *30*, 12941–12949.
19. Luong, H.M.; Pham, M.T.; Guin, T.; Madhogaria, R.P.; Phan, M.-H.; Larsen, G.K.; Nguyen, T.D. Sub-second and ppm-level optical sensing of hydrogen using templated control of nano-hydride geometry and composition. *Nat. Commun.* **2021**, *12*, 2414.
20. Archer, R.J.; Parnell, A.J.; Campbell, A.I.; Howse, J.R.; Ebbens, S.J. A Pickering emulsion route to swimming active Janus colloids. *Adv. Sci.* **2018**, *5*, 1700528.
21. Lyu, Z.; Yao, L.; Wang, Z.; Qian, C.; Wang, Z.; Li, J.; Liu, C.; Wang, Y.; Chen, Q. Nanoscopic imaging of self-propelled ultrasmall catalytic nanomotors. *ACS Nano* **2024**, *18*, 14231–14243.
22. Wang, X.; Liu, B. Molecular alignment-induced chemically patchy uniaxial nanoparticles and their applications in anti-counterfeiting and self-assembled superstructures. *Angew. Chem. Int. Ed.* **2023**, *62*, e202218399.
23. Cao, Q.; Han, S.-J.; Tersoff, J.; Franklin, A.D.; Zhu, Y.; Zhang, Z.; Tulevski, G.S.; Tang, J.; Haensch, W. End-bonded contacts for carbon nanotube transistors with low, size-independent resistance. *Science* **2015**, *350*, 68–72.
24. Qin, D.; Xia, Y.; Whitesides, G.M. Soft lithography for micro-and nanoscale patterning. *Nat. Protoc.* **2010**, *5*, 491–502.
25. Suh, H.S.; Kim, D.H.; Moni, P.; Xiong, S.; Ocola, L.E.; Zaluzec, N.J.; Gleason, K.K.; Nealey, P.F. Sub-10-nm patterning via directed self-assembly of block copolymer films with a vapour-phase deposited topcoat. *Nat. Nanotechnol.* **2017**, *12*, 575–581.
26. De Gennes, P. *Scaling Concepts in Polymer Physics*; Cornell University Press: Ithaca, NY, USA, 1979.
27. Choueiri, R.M.; Galati, E.; Thérien-Aubin, H.; Klinkova, A.; Larin, E.M.; Querejeta-Fernández, A.; Han, L.; Xin, H.L.; Gang, O.; Zhulina, E.B.; et al. Surface patterning of nanoparticles with polymer patches. *Nature* **2016**, *538*, 79–83.
28. Galati, E.; Tao, H.; Tebbe, M.; Ansari, R.; Rubinstein, M.; Zhulina, E.B.; Kumacheva, E. Helicoidal patterning of nanorods with polymer ligands. *Angew. Chem. Int. Ed.* **2019**, *58*, 3123–3127.
29. Galati, E.; Tebbe, M.; Querejeta-Fernández, A.; Xin, H.L.; Gang, O.; Zhulina, E.B.; Kumacheva, E. Shape-specific patterning of polymer-functionalized nanoparticles. *ACS Nano* **2017**, *11*, 4995–5002.
30. Rodríguez-Fernández, J.; Pérez-Juste, J.; Mulvaney, P.; Liz-Marzán, L.M. Spatially-directed oxidation of gold nanoparticles by Au(III)−CTAB complexes. *J. Phys. Chem. B* **2005**, *109*, 14257–14261.
31. Schlenoff, J.B.; Li, M.; Ly, H. Stability and self-exchange in alkanethiol monolayers. *J. Am. Chem. Soc.* **1995**, *117*, 12528–12536.
32. Yang, G.; Amro, N.A.; Starkewolfe, Z.B.; Liu, G.-y. Molecular-level approach to inhibit degradations of alkanethiol self-assembled monolayers in aqueous media. *Langmuir* **2004**, *20*, 3995–4003.
33. Galati, E.; Tao, H.; Rossner, C.; Zhulina, E.B.; Kumacheva, E. Morphological transitions in patchy nanoparticles. *ACS Nano* **2020**, *14*, 4577–4584.
34. Rossner, C.; Zhulina, E.B.; Kumacheva, E. Staged surface patterning and self-assembly of nanoparticles functionalized with end-grafted block copolymer ligands. *Angew. Chem. Int. Ed.* **2019**, *58*, 9269–9274.
35. Duan, H.; Luo, Q.; Wei, Z.; Lin, Y.; He, J. Symmetry-broken patches on gold nanoparticles through deficient ligand exchange. *ACS Macro Lett.* **2021**, *10*, 786–790.
36. Duan, H.; Malesky, T.; Wang, J.; Liu, C.-H.; Tan, H.; Nieh, M.-P.; Lin, Y.; He, J. Patchy metal nanoparticles with polymers: Controllable growth and two-way self-assembly. *Nanoscale* **2022**, *14*, 7364–7371.
37. Duan, H.; Jia, Z.; Liaqat, M.; Mellor, M.D.; Tan, H.; Nieh, M.-P.; Lin, Y.; Link, S.; Landes, C.F.; He, J. Site-specific chemistry on gold nanorods: Curvature-guided surface dewetting and supracolloidal polymerization. *ACS Nano* **2023**, *17*, 12788–12797.

38. Yang, Y.; Yi, C.; Duan, X.; Wu, Q.; Zhang, Y.; Tao, J.; Dong, W.; Nie, Z. Block-random copolymer-micellization-mediated formation of polymeric patches on gold nanoparticles. *J. Am. Chem. Soc.* **2021**, *143*, 5060–5070.
39. Singh, C.; Ghorai, P.K.; Horsch, M.A.; Jackson, A.M.; Larson, R.G.; Stellacci, F.; Glotzer, S.C. Entropy-mediated patterning of surfactant-coated nanoparticles and surfaces. *Phys. Rev. Lett.* **2007**, *99*, 226106.
40. Ghorai, P.K.; Glotzer, S.C. Atomistic simulation study of striped phase separation in mixed-ligand self-assembled monolayer coated nanoparticles. *J. Phys. Chem. C* **2010**, *114*, 19182–19187.
41. Chen, T.; Yang, M.; Wang, X.; Tan, L.H.; Chen, H. Controlled assembly of eccentrically encapsulated gold nanoparticles. *J. Am. Chem. Soc.* **2008**, *130*, 11858–11859.
42. Chen, G.; Gibson, K.J.; Liu, D.; Rees, H.C.; Lee, J.-H.; Xia, W.; Lin, R.; Xin, H.L.; Gang, O.; Weizmann, Y. Regioselective surface encoding of nanoparticles for programmable self-assembly. *Nat. Mater.* **2019**, *18*, 169–174.
43. Tao, H.; Chen, L.; Galati, E.; Manion, J.G.; Seferos, D.S.; Zhulina, E.B.; Kumacheva, E. Helicoidal patterning of gold nanorods by phase separation in mixed polymer brushes. *Langmuir* **2019**, *35*, 15872–15879.
44. Song, X.; Zhang, X.; Ou, Z.; Zhang, Y.-Q.; Li, M. Controlling the anisotropic surface wetting of metal nanoparticles by a competitive ligand packing strategy: Implications for encapsulation. *ACS Appl. Nano Mater.* **2021**, *4*, 11458–11465.
45. Zhou, J.; Creyer, M.N.; Chen, A.; Yim, W.; Lafleur, R.P.; He, T.; Lin, Z.; Xu, M.; Abbasi, P.; Wu, J. Stereoselective growth of small molecule patches on nanoparticles. *J. Am. Chem. Soc.* **2021**, *143*, 12138–12144.
46. Wang, Z.; He, B.; Xu, G.; Wang, G.; Wang, J.; Feng, Y.; Su, D.; Chen, B.; Li, H.; Wu, Z. Transformable masks for colloidal nanosynthesis. *Nat. Commun.* **2018**, *9*, 563.
47. Song, X.; Liu, C.; Liu, X.; Liu, S. Investigating polymer transformation during the encapsulation of metal nanoparticles by polystyrene-*b*-poly(acrylic acid) in colloids. *ACS Appl. Mater. Interfaces* **2019**, *12*, 3969–3975.
48. Kim, J.; Song, X.; Kim, A.; Luo, B.; Smith, J.W.; Ou, Z.; Wu, Z.; Chen, Q. Reconfigurable polymer shells on shape-anisotropic gold nanoparticle cores. *Macromol. Rapid Commun.* **2018**, *39*, 1800101.
49. Santos, A.; Millan, J.A.; Glotzer, S.C. Facetted patchy particles through entropy-driven patterning of mixed ligand SAMS. *Nanoscale* **2012**, *4*, 2640–2650.
50. Kim, A.; Zhou, S.; Yao, L.; Ni, S.; Luo, B.; Sing, C.E.; Chen, Q. Tip-patched nanoprisms from formation of ligand islands. *J. Am. Chem. Soc.* **2019**, *141*, 11796–11800.
51. Kim, A.; Vo, T.; An, H.; Banerjee, P.; Yao, L.; Zhou, S.; Kim, C.; Milliron, D.J.; Glotzer, S.C.; Chen, Q. Symmetry-breaking in patch formation on triangular gold nanoparticles by asymmetric polymer grafting. *Nat. Commun.* **2022**, *13*, 6774.
52. Yao, L.; An, H.; Zhou, S.; Kim, A.; Luijten, E.; Chen, Q. Seeking regularity from irregularity: Unveiling the synthesis–nanomorphology relationships of heterogeneous nanomaterials using unsupervised machine learning. *Nanoscale* **2022**, *14*, 16479–16489.
53. Kherbouche, I.; MacRae, D.; Jourdain, T.G.; Lagugné-Labarthet, F.; Lamouri, A.; Biraud, A.C.; Mangeney, C.; Félidj, N. Extending nanoscale patterning with multipolar surface plasmon resonances. *Nanoscale* **2021**, *13*, 11051–11057.
54. Ji, Y.; Lin, X.; Wu, Z.; Wu, Y.; Gao, W.; He, Q. Macroscale chemotaxis from a swarm of bacteria-mimicking nanoswimmers. *Angew. Chem. Int. Ed.* **2019**, *58*, 12200–12205.
55. Ohnuma, A.; Cho, E.C.; Camargo, P.H.; Au, L.; Ohtani, B.; Xia, Y. A facile synthesis of asymmetric hybrid colloidal particles. *J. Am. Chem. Soc.* **2009**, *131*, 1352–1353.
56. Ohnuma, A.; Cho, E.C.; Jiang, M.; Ohtani, B.; Xia, Y. Metal−polymer hybrid colloidal particles with an eccentric structure. *Langmuir* **2009**, *25*, 13880–13887.
57. Nie, Z.; Fava, D.; Kumacheva, E.; Zou, S.; Walker, G.C.; Rubinstein, M. Self-assembly of metal−polymer analogues of amphiphilic triblock copolymers. *Nat. Mater.* **2007**, *6*, 609–614.
58. Kim, A.; Akkunuri, K.; Qian, C.; Yao, L.; Sun, K.; Chen, Z.; Vo, T.; Chen, Q. Direct imaging of “patch-clasping” and relaxation in robust and flexible nanoparticle assemblies. *ACS Nano* **2024**, *18*, 939–950.
59. Hiemenz, P.C.; Rajagopalan, R. *Principles of Colloid and Surface Chemistry, Revised and Expanded*; CRC Press: Boca Raton, FL, USA, 2016.
60. Israelachvili, J.N. *Intermolecular and Surface Forces*; Academic Press: Cambridge, MA, USA, 2011.
61. Li, Y.; Zhou, W.; Tanriover, I.; Hadibrata, W.; Partridge, B.E.; Lin, H.; Hu, X.; Lee, B.; Liu, J.; Dravid, V.P. Open-channel metal particle superlattices. *Nature* **2022**, *611*, 695–701.
62. Dong, Y.; Liu, J.; Lu, X.; Duan, J.; Zhou, L.; Dai, L.; Ji, M.; Ma, N.; Wang, Y.; Wang, P. Two-stage assembly of nanoparticle superlattices with multiscale organization. *Nano Lett.* **2022**, *22*, 3809–3817.
63. Lewis, D.J.; Carter, D.J.; Macfarlane, R.J. Using DNA to control the mechanical response of nanoparticle superlattices. *J. Am. Chem. Soc.* **2020**, *142*, 19181–19188.
64. Lu, F.; Vo, T.; Zhang, Y.; Frenkel, A.; Yager, K.G.; Kumar, S.; Gang, O. Unusual packing of soft-shelled nanocubes. *Sci. Adv.* **2019**, *5*, eaaw2399.
65. Tan, L.H.; Xing, H.; Chen, H.; Lu, Y. Facile and efficient preparation of anisotropic DNA-functionalized gold nanoparticles and their regioselective assembly. *J. Am. Chem. Soc.* **2013**, *135*, 17675–17678.

66. Qiu, J.; Xie, M.; Lyu, Z.; Gilroy, K.D.; Liu, H.; Xia, Y. General approach to the synthesis of heterodimers of metal nanoparticles through site-selected protection and growth. *Nano Lett.* **2019**, *19*, 6703–6708.
67. Woessner, Z.J.; Lewis, G.R.; Bueno, S.L.; Ringe, E.; Skrabalak, S.E. Asymmetric seed passivation for regioselective overgrowth and formation of plasmonic nanobowls. *Nanoscale* **2022**, *14*, 16918–16928.
68. Huang, Z.; Liu, Y.; Zhang, Q.; Chang, X.; Li, A.; Deng, L.; Yi, C.; Yang, Y.; Khashab, N.M.; Gong, J.; et al. Collapsed polymer-directed synthesis of multicomponent coaxial-like nanostructures. *Nat. Commun.* **2016**, *7*, 12147.
69. Yan, M.; Liu, T.; Li, X.; Zhou, S.; Zeng, H.; Liang, Q.; Liang, K.; Wei, X.; Wang, J.; Gu, Z. Soft patch interface-oriented superassembly of complex hollow nanoarchitectures for smart dual-responsive nanospacecrafts. *J. Am. Chem. Soc.* **2022**, *144*, 7778–7789.
70. Li, L.; Yang, Y.; Ding, J.; Xue, J. Synthesis of magnetite nanooctahedra and their magnetic field-induced two-/three-dimensional superstructure. *Chem. Mater.* **2010**, *22*, 3183–3191.
71. Coropceanu, I.; Rossinelli, A.; Caram, J.R.; Freyria, F.S.; Bawendi, M.G. Slow-injection growth of seeded CdSe/CdS nanorods with unity fluorescence quantum yield and complete shell to core energy transfer. *ACS Nano* **2016**, *10*, 3295–3301.
72. Chen, W.; Zhan, X.; Luo, B.; Ou, Z.; Shih, P.-C.; Yao, L.; Pidaparthy, S.; Patra, A.; An, H.; Braun, P.V. Effects of particle size on Mg^{2+} ion intercalation into λ-MnO_2 cathode materials. *Nano Lett.* **2019**, *19*, 4712–4720.
73. Cargnello, M.; Wieder, N.L.; Canton, P.; Montini, T.; Giambastiani, G.; Benedetti, A.; Gorte, R.J.; Fornasiero, P. A versatile approach to the synthesis of functionalized thiol-protected palladium nanoparticles. *Chem. Mater.* **2011**, *23*, 3961–3969.
74. Wang, Y.; Im, J.; Soares, J.W.; Steeves, D.M.; Whitten, J.E. Thiol adsorption on and reduction of copper oxide particles and surfaces. *Langmuir* **2016**, *32*, 3848–3857.
75. Melby, E.S.; Lohse, S.E.; Park, J.E.; Vartanian, A.M.; Putans, R.A.; Abbott, H.B.; Hamers, R.J.; Murphy, C.J.; Pedersen, J.A. Cascading effects of nanoparticle coatings: Surface functionalization dictates the assemblage of complexed proteins and subsequent interaction with model cell membranes. *ACS Nano* **2017**, *11*, 5489–5499.
76. Na, H.B.; Palui, G.; Rosenberg, J.T.; Ji, X.; Grant, S.C.; Mattoussi, H. Multidentate catechol-based polyethylene glycol oligomers provide enhanced stability and biocompatibility to iron oxide nanoparticles. *ACS Nano* **2012**, *6*, 389–399.